Subdivision Directional Field Processing

An MSc thesis by Bram Custers

Supervisor Amir Vaxman Second examiner Maarten Löffler

Utrecht University

Faculty of Science
Department of Information and Computing Sciences
ICA-3812561
September 12, 2018

Abstract

We present a novel subdivision scheme for face-based tangent directional fields on triangle meshes. Our subdivision scheme is based on a novel coordinate-free representation of directional fields as halfedge-based scalar quantities, bridging the finite-element representation of fields with that of discrete exterior calculus. By commuting with differential operators, our subdivision is structure-preserving: it reproduces curl-free fields exactly, and divergence-free fields in the weak sense. Moreover, our scheme directly extends to fields with several vectors per face. Finally, we show how our scheme is useful for applications that need robust and efficient face-based directional field processing, such as advection, robust earth mover's distance computation, and directional-field design.

Contents

1. Introduction

Directional fields are some of the most important objects in geometry processing. They represent flows, alignments, and symmetry on discrete meshes. They are used for diverse applications, such as meshing, fluid simulation, texture synthesis, architectural design, and many more. As such, there is great value in producing robust and reliable algorithms to design and analyze such fields. In this paper, we work with piecewise-constant tangent directional fields, defined on the faces of a triangle mesh. A general directional field is the assignment of several vectors per face, where the most commonly-used fields comprise single vectors. The representation of directional fields as piecewise-constant and face-based is one of the mainstream representations for the *finite-element method* (**FEM**), where such vectors are gradients of piecewise-linear functions on the mesh elements.

Unfortunately, the piecewise-constant representation is very sensitive to the quality of the mesh and its resolution. A mesh that is too coarse or uneven would break the robustness of most applications and produce wrong results. One might alleviate such a problem by working with a fine (and good-quality) mesh. However, working on a fine mesh would be computationally expensive, and often wasteful—the desired directional fields are likely smooth and mostly defined by key features such as sinks, sources, and vorticity.

A classical way to bridge this gap is to work with a multi-resolution structure, by creating a hierarchy of meshes. A popular way to do so in geometry processing is to use *subdivision surfaces*, where the meshes are refinable by a set of linear and stationary stencils. Then, one needs to define subdivision operators for directional fields represented on these meshes. A necessary requirement for the consistency of the results is that the subdivision is *structure-preserving*; that is, the differential and topological properties of the directional fields should be preserved under subdivision; for this, the subdivision operators are required to commute with differential operators. Unfortunately, the differential operators on piecewise-constant face-based fields are defined on the embedding directly, and the metric and embedding properties of the subdivided triangulation (such as face area and normals) have complicated and nonlinear expressions with relation to linear subdivision operators on the coordinates of the vertices. That means that creating subdivision operators directly on face-based directional fields is a difficult challenge.

Recently, deGoes *et al.* [2016b] devised a subdivision method for differential forms in the *discrete exterior calculus* (**DEC**) setting. The differential quantities in DEC are clearly separated into combinatorial and metric operators; due to this, they could define a subdivision for differential forms commuting with the combinatorial part alone, and obtain stationary and local schemes.

Inspired by this technique, we introduce a coordinate-free representation for face-based fields, allowing us to decompose the FEM differential operators into independent combinatorial and metric components. Consequently, we establish subdivision schemes for face-based fields. Our subdivision extends to general directional fields, for any number of vectors per face.

In summary, our contributions are the folllowing:

- We introduce a coordinate-free representation for face-based directional fields, based on halfedge scalar quantities. Subsequently, we create equivalent definitions for all vector-calculus differential operators on this representation.
- We define a subdivision scheme for this representation that commutes with the differential operators, allowing for structure-preserving directional-field subdivision.
- We show how our scheme allows for coarse-to-fine directional field processing, where fields on fine meshes are computed directly on the coarse mesh.
- We demonstrate that our scheme extends to general directional fields with N vectors per face.

We demonstrate the utility and effectiveness of our subdivision scheme for directional-field design, discrete function advection, and distance computation on meshes.

2. Related work

1 DIRECTIONAL FIELDS

Tangent directional fields on discrete meshes have been extensively studied in recent years. The important aspects of their design and analysis are summarized in two relevant surveys: [de Goes et al. 2016a] focuses on differential properties of mostly single vector fields, with an emphasis on different discretizations of meshes, while [Vaxman et al. 2016] focuses on discretization and representation of directional fields (with N vectors at every given tangent plane) and their applications.

The fundamental challenge of working with directional fields is how to discretize and represent them. The most common discretization considers one directional object per face, or alternatively piecewise-constant elements (e.g., [Bommes et al. 2009; Crane et al. 2010; Tong et al. 2003; Wardetzky 2006]). This representation conforms with the classic piecewise linear paradigm of the finite-element method, and admits a dimensionality-correct cohomological structure, when mixing conforming and non-conforming elements [Wardetzky 2006]. Moreover, the natural tangent planes, as supporting plane to the triangles in the mesh, allows for simple representations of N-directional fields [Crane et al. 2010; Diamanti et al. 2014; Knöppel et al. 2013; Ray et al. 2008]. However, the representation is only C^0 smooth, and makes it difficult to define discrete operators of higher order including derivatives of directional fields, such as the Lie bracket [Azencot et al. 2013; Mullen et al. 2011], or Killing fields [Ben-Chen et al. 2010]. An alternative approach to *vector*-field processing is *discrete exterior calculus* (DEC) [Crane et al. 2013; Hirani 2003], which considers vector fields as 1-forms, represented as scalars on edges. DEC enjoys the benefit of representing fields in a coordinate-free manner, which allows for simpler construction of differential operators in some cases (such as the subdivision one we use in this paper). However, DEC is not as of yet defined to work with general directional fields, and when using it with linear Whitney forms, it still suffers from discontinuities at edges and vertices. We note that alternative approaches exist that use vertex-based definitions [Knöppel et al. 2013; Liu et al. 2016; Zhang et al. 2006], which represent directional fields on intrinsic tangent planes defined at vertices. While enjoying better continuity, a full suite of differential operators has not been studied for them, in particular the existence of a discrete exact sequence, necessary for a correct Helmholtz-Hodge decomposition [Poelke and Polthier 2016; Wardetzky 2006].

2 MULTIRESOLUTION VECTOR CALCULUS

Directional fields are important for applications such as meshing [Bommes et al. 2009; Kälberer et al. 2007; Zadravec et al. 2010], simulations on surfaces [Azencot et al. 2015], parameterization [Campen et al. 2015; Diamanti et al. 2015; Myles and Zorin 2012] and non-photorealistic rendering [Hertzmann and Zorin 2000]. An underlying objective in all these applications is to obtain fields that are as smooth as possible. Nevertheless, as demonstrated in [Vaxman et al. 2016], directional fields are subject to aliasing and noise artefacts quite easily for coarse meshes. Using fine meshes alleviates this problem to some extent, but incurs a price of increased computational overhead, especially for nonlinear methods. For this, a smooth and low-dimensional representation for smooth directional fields on fine meshes, like the one we present in this paper, is much needed.

The most prevalent approach to low-dimensional smooth processing on fine meshes is to use some refinable multi-resolution hierarchy. This paradigm is extensively employed in the FEM literature when using either refined elements (*h-refinement*) or higher-order basis functions (*p-refinement*) [Babuška and Suri 1994]. This has also been applied to vector fields in the plane and in volumes. However, such approaches do not generalize directly to curved surfaces in which the limit surface is different than the cage. As such, they are susceptible to committing the so-called "variational crime" [Strang and Fix 2008], where the function space and the computation domain are mismatched.

A prominent recent approach to refinable elements is *Isogeometric Analysis* [Hughes et al. 2005]. The premise is computation over refinable B-spline basis functions, replacing the piecewise-linear FEM functions. The setting uses exact integration over the target smooth domain, and therefore is theoretically robust. However, they rely on quadrature rules to perform the complicated integrals that involve the basis functions [Jüttler et al. 2016; Nguyen et al. 2014]. As such, they are not easily extensible to irregular domains such as arbitrary triangle meshes. Moreover, working on the limit surface does not guarantee structure-preservation for any intermediate discrete level.

A recent work by deGoes *et al.* [2016b] utilized subdivision for 1-forms (first introduced in [Wang et al. 2006]) as means to represent vector-field in recursively refinable spaces. By doing so, they efficiently emulate the IGA premise in a linear setting, and directly on the discrete meshes. This technique replaced coarse inner product matrices with coarsened inner product matrices

on the fine domains, encoding their geometry. By treating the subdivision matrix as a prolongation operator, this is akin to collapsing a single V-cycle in a multigrid setting [Brandt 1977]. The idea behind the technique was to create stationary subdivision matrices that commute with the discrete differential operators. This is made possible due to the fact that the operators are purely combinatorial.

Unfortunately, their approach does not easily extend to face-based piecewise-constant fields. The effect of stationary subdivision methods on the triangle area and normal are not linear, which makes it difficult to establish the required commutation rules. Our paper introduces a novel representation of face-based fields using halfedge-based forms, that can be readily subdivided using stationary operators. As such, we introduce a metric-free subdivision method for face-based directional fields with guarantees the structure-preservation.

We note that the nested spaces can be used to encode progressive details over subdivision surfaces. This is the motivation of constructing *subdivision wavelets* [Bertram 2004; Lounsbery et al. 1997] over subdivision surfaces.

3 SUBDIVISION SURFACES IN GEOMETRY PROCESSING

Subdivision surfaces are popular objects in geometry processing, and are a preferred method for shape design for animation [Liu et al. 2014] and architectural geometry [Liu et al. 2006]. Their most popular utility is that of multiresolution (or just coarse-to-fine) mesh editing. However, they have been applied to fluid simulation [Stam 2003], and surface deformation [Grinspun et al. 2002; Thomaszewski et al. 2006]. In addition, they also use the folded V-cycle approach to work on the coarse mesh while using the limit surface metric; nevertheless, they work with quadrature as well, and therefore lack the same guarantees for preserving structure.

3. Background

1 FUNCTION SPACES

We work with a mesh $\mathcal{M} = \{V, E, F\}$. As we combine FEM and DEC formulations, we need to streamline notation at the expense of conventionality. We summarize the spaces we employ in Figure 1. We define $\mathcal{V}$ as the space of piecewise-linear (conforming) vertex-based functions, corresponding to 0-forms with linear Whitney forms in DEC and $\mathcal{S}_h$ in FEM. We further define $\mathcal{E}$ as the space of piecewise-linear mid-edge (non-conforming) functions, also known as the *Crouzeix-Raviart* elements [Crouzeix and Raviart 1973], corresponding to $\mathcal{S}_h^*$ in FEM. We define $\mathcal{F}$ as the space of piecewise-constant functions on faces, corresponding with dual 2-forms in DEC. We define the corresponding integrated (weak) function spaces on vertices as $\mathcal{V}^*$ (corresponding to dual 0-forms), on edges as $\mathcal{E}^*$ (defined on edge diamond areas), and on faces as $\mathcal{F}^*$ (corresponding to primal 2-forms in DEC). Finally, we use $\mathcal{Z}_1$ for DEC-based 1-forms, and $\mathcal{X}^N$ for *piecewise-constant directional fields* (**PCDF**) of degree N defined on the tangent spaces spanned by the supporting plane to each face. These latter definitions are in accordance with the respective conventional notation. We introduce our operators to the classic case of $N = 1$, and then generalize our constructions to N-directional fields in Section 2.3. For that case, we omit the power and just use $\mathcal{X}$,the space of piecewise-constant vector fields (**PCVF**).

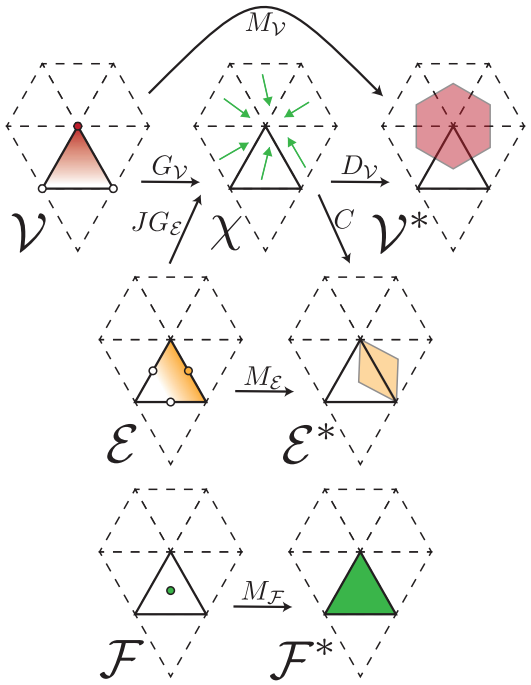

Fig. 1. The FEM function spaces and associated differential operators.

2 FEM DIFFERENTIAL OPERATORS

We give a concise description of well-known discrete differential operators. For deeper analysis of these operators and their properties, we refer the reader to [Wardetzky 2006] and [de Goes et al. 2016a]. We use the notation of Figure 2 throughout this section.

Discrete gradient. We define the discrete conforming gradient $G_{\mathcal{V}} : \mathcal{V} \to \chi$ of a function $f : \mathcal{V} \to \mathbb{R}$, restricted to a face $t = ijk$ (without loss of generality) as follows:

$$G_{\mathcal{V}|t} \begin{pmatrix} f_i \\ f_j \\ f_k \end{pmatrix} = \frac{1}{2A_{ijk}} \begin{pmatrix} e_{jk}^{\perp} \\ e_{ki}^{\perp} \\ e_{ij}^{\perp} \end{pmatrix}^T \begin{pmatrix} f_i \\ f_j \\ f_k \end{pmatrix}, \tag{1}$$

where A_{ijk} is the area of t, and $e_{ij}^{\perp} = n_{ijk} \times e_{ij}$ (a rotation of the edge ij around the normal to ijk, as a row vector, and similarly for jk and ki). We aggregate the per-face contributions into a matrix $G_{\mathcal{V}} : 3\,|F| \times |V|$.

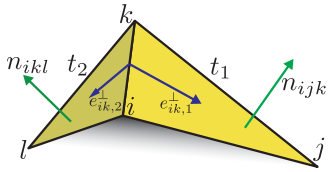

Fig. 2. Notation for a single flap.

Non-conforming gradient. The non-conforming gradient, or *cogradient* $G_{\mathcal{E}} : \mathcal{E} \to \chi$ of a mid-edge function $g : \mathcal{E} \to \mathbb{R}$ is defined as:

$$G_{\mathcal{E},|t} \begin{pmatrix} g_{ij} \\ g_{jk} \\ g_{ki} \end{pmatrix} = -\frac{1}{A_{ijk}} \begin{pmatrix} e_{ij}^{\perp} \\ e_{jk}^{\perp} \\ e_{ki}^{\perp} \end{pmatrix}^T \begin{pmatrix} g_{ij} \\ g_{jk} \\ g_{ki} \end{pmatrix}. \tag{2}$$

This is essentially similar to $G_{\mathcal{V}}$ (as conforming functions are a subset of non-conforming functions). We are usually interested in *rotated cogradients*. For a face f We define $J_{|f} = \left[n_f \times\right]$ as the operator that performs the rotation around the normal. The operator J aggregates these local matrices. Then, the rotated cogradient is the operator $JG_{\mathcal{E}}$.

Discrete non-conforming curl. We consider the weak (integrated) non-conforming curl operator $C : \mathcal{X} \to \mathcal{E}^*$, operating on a vector field $v \in \chi$, defined as follows:

$$C_{|ik} \cdot v = \langle v_{ijk}, e_{ik} \rangle - \langle v_{ikl}, e_{ik} \rangle \tag{3}$$

Note that the definition seems orientation dependent, but it is not: the direction of the edge e_{ik} (rather than e_{ki}) is arbitrary, but then we must use the correct direction of the *dual* edge $ijk \to ikl$. The curl itself is then orientation-independent, as a quantity in $\mathcal{E}^*$.

Discrete conforming divergence. We consider the integrated conforming divergence operator $D : \mathcal{X} \to \mathcal{V}^*$, defined on vertex i as follows:

$$D_{|i} = \frac{1}{2} \sum_{ijk \in N_i} \langle v_{ijk}, e_{jk}^{\perp} \rangle = \left(G_{\mathcal{V}}\right)^T \cdot M_{\mathcal{F}} \tag{4}$$

where N_i is the set of triangles adjacent to vertex i. $M_{\mathcal{F}}$ is the mass matrix of space $\mathcal{F}$, comprising diagonal values of triangle areas.

Helmhold-Hodge decomposition. For a closed surface without boundary, there is a well-defined Helmholtz-Hodge decomposition of $\mathcal{X}$ as follows:

$$\mathcal{X} = Image\left\{G_{\mathcal{V}}\right\} \oplus Image\left\{JG_{\mathcal{E}}\right\} \oplus \mathcal{H}_{\chi}. \tag{5}$$

$ImageG_{\mathcal{V}}$ is the space of vectors fields that are gradients of functions in $\mathcal{V}$, $ImageJG_{\mathcal{E}}$ the space of rotated cogradients of functions in $\mathcal{E}$, and $\mathcal{H}$ is the space of *harmonic fields*, which has dimension $2g$, where g is the genus of the mesh.

Mixing spaces. It is well-known [Polthier and Preuß 2003; Wardetzky 2006] that Image$G_{\mathcal{V}} \subset \ker C$ (gradient fields are curl-free) and and that Image$JG_{\mathcal{E}} \subset \ker D$ (rotated *cogradient* fields are divergence free). As a consequence, we get $\mathcal{H} = \ker C\ \ker D$. The mixing of conforming and non-conforming operators is essential for creating an consistent exact sequence, and dimensionality-correct Hodge decomposition . The entire formulation can be done in a dual manner by switching conforming and non-conforming spaces and operators, butr we will restrict ourselves to conforming gradients and non-conforming rotated cogradients.

Inner products. Inner products on the function spaces are encoded as mass matrices M, where two elements u, v in column vector form in some function space $\mathcal{P}$ have the inner product $\langle u, v \rangle_{\mathcal{P}} = u^T M_{\mathcal{P}} v$. We already defined $M_{\mathcal{F}}$ above, and we further define $M_{\mathcal{V}}$ to be the diagonal matrix of *Voronoi areas* of every vertex, and $M_{\mathcal{E}}$ to be the diagonal matrix of *diamond areas* supported on each edge (See Figure 1). Mass matrices for dual forms are the inverses to the mass matrices of the corresponding primal form. We note that $M_{\mathcal{V}}$ and $M_{\mathcal{E}}$ are in fact *lumped* versions, so that they are diagonal, and have simple inverses.

The Laplacian. The well-known conforming integrated Laplacian operator $L_{\mathcal{V}} : \mathcal{V} \to \mathcal{V}^*$ is defined in FEM as $L_{\mathcal{V}} = DG_{\mathcal{V}} = G_{\mathcal{V}}^T M_{\mathcal{F}} G_{\mathcal{V}}$. Note that it reveals the nature of the Laplacian matrix as an inner-product matrix of the form $\langle \nabla f_1, \nabla f_2 \rangle$ for vertex-based functions $f_1, f_2 \in \mathcal{V}$. The result is the *cotangent Laplacian*:

$$\left(L_{\mathcal{V}}\right)_{ik} = \left\{ \begin{array}{ll} i = k & \left(i,k\right) \in E \, w_{ik} \\ i \neq k & -w_{ik} \end{array} \right\}, \tag{6}$$

where $w_{ik} = \frac{cot\angle ijk + cot\angle kli}{2}$. The non-conforming Laplacian $L_{\mathcal{E}}$ is consequently

$$L_{\mathcal{E}} = G_{\mathcal{E}} J^T M_{\mathcal{F}} J G_{\mathcal{E}} = G_{\mathcal{E}}^T M_{\mathcal{F}} G_{\mathcal{E}}.$$

The pointwise versions of these Laplacians are $\left(M_{\mathcal{V}}\right)^{-1} L_{\mathcal{V}}$ and $\left(M_{\mathcal{E}}\right)^{-1} L_{\mathcal{E}}$.

3 DISCRETE EXTERIOR CALCULUS

We choose an arbitrary (but fixed) orientation for every edge in the mesh. This orientation consistently defines both source and target vertices, and left and right faces for each edge. For instance, in our notation, we use e_{ik} and get $lefte_{ik} = ikl$ and $righte_{ik} = ijk$. For edge e and adjacent face f, we define $s_{e,f} = \pm 1$ as the sign encoding the orientation (positive if $f = righte$).

DEC function spaces. The setup of DEC [Desbrun et al. 2005] is an alternative to the FEM piecewise-constant representation described in the previous section. Instead of representing vectors explicitly, DEC works with primal and dual k-forms, where primal 0-forms are (pointwise) vertex-based functions, primal 1-forms are (integrated) edge-based functions (representing vectors), and primal 2-forms are (integrated) face based functions. The space of primal 0 forms $\mathcal{Z}_0$, with the interpolation of *Whitney forms*, identifies with $\mathcal{V}$. The space of 1-forms $\mathcal{Z}_1$ comprises scalars on edges, representing oriented quantities. Such quantities are oriented in the sense that when a scalar z is attached to edge e_{ik}, then the corresponding scalar for the edge e_{ki} is $-z$. Note that the FEM spaces $\mathcal{E}$ and $\mathcal{E}^*$ do not have this property, as they are invariant to the orientation of the edge, and therefore do not identify with $\mathcal{Z}_1$. The space of 2-forms $\mathcal{Z}_2$ identifies with $\mathcal{F}^*$ (note the duality, as elements in $\mathcal{Z}_2$ are integrated).

The space of dual 0-forms $\mathcal{Z}_0^*$ are integrated vertex-based quantities, and identifies with $\mathcal{V}^*$. Similarly, $\mathcal{Z}_2^*$ identifies with $\mathcal{F}$. Dual 1-forms in the space $\mathcal{Z}_1^*$ are defined on the union of the orthogonal duals to edge ik in triangles ijk and ikl. Such duals are perpendicular bisectors e_{ik}^* to e_{ik} from the center of the circumscribing circles, and are therefore different in length than $e_{ik}^{\perp}$ (in either face).

Differential operators. Two fundamental discrete operators are combined to create an entire suite of vector calculus: the differential d, taking k-forms into $\left(k+1\right)$-forms, and the Hodge star $\star$, taking primal k-forms into dual $2-k$ dual forms (on surface meshes). For instance, $\star_1 : \mathcal{Z}_1 \to \mathcal{Z}_1^*$ is defined as $\star_{|ik,1} = \frac{\left|e_{ik}^*\right|}{\left|e_{ik}\right|}$. To streamline notation, we use M_1 to represent $\star_1$. $M_1 : |E| \times |E|$ is a diagonal matrix that contains the cotangent weights per edge, as defined in Section 2. M_0 identifies with $M_{\mathcal{V}}$, as a diagonal matrix of Voronoi areas. However, note that M_2 identifies with M_f^{-1} by convention (since primal 2-forms are integrated).

The de-Rham exact sequence of DEC is also achieved as $d^2 = 0$ in the discrete setting, and therefore DEC is also structure preserving. In the dual setting, we also work with the coboundary operator $\partial = d^T$. Intuitively, this operator sums up $\left(k+1\right)$-forms into k-forms of elements (chains) adjacent to them, with relation to the mutual orientation. The vector calculus operators are then interpreted as follows: the curl operator is simply d_1, where curl is a primal 2-form in DEC, and primal (weak) divergence is $\left(d_0\right)^T M_1$, producing a dual 0-form.

Curl-free 1-forms, where $d_1 z_1 = 0$ are called *closed*, and 1-forms z_1 for which there exists a 0-form z_0 so that $z_1 = d_0 z_0$ are called *exact* (paralleling the notion of gradient fields in FEM). It is evident that exact forms are by definition closed. Divergence-free 1-forms, where $d_0^T M_1 z_1 = 0$ are called coclosed, and 1-forms for which exists a 2-form such that $z_1 = M_1^{-1} \left(d_1\right)^T M_2 z_2$ are called *coexact* (paralleling cogradient fields in FEM). In general, we have a Hodge decomposition for 1-forms, where for each $z_1 \in \mathcal{Z}_1$ there exist $z_0 \in \mathcal{Z}_0$ and $z_2 \in \mathcal{Z}_2$ such that:

$$z_1 = d_0 z_0 + M_1^{-1} d_1^T M_2 z_2 + h_1. \tag{7}$$

where h_1 is a harmonic 1-form that is both closed and coclosed.

The 0-form Laplacian in DEC is then $L_0 = d_0^T M_1 d_0$. It is evident that this is equivalent to $L_{\mathcal{V}}$, as M_1 contains cotangent weights, and from the combinatorial structure of d_0.

Between DEC and FEM. As linear discrete frameworks, DEC and FEM admit a similar power of expression, for instance $L_0 = L_{\mathcal{V}}$. However, they are incompatible otherwise; $|\mathcal{Z}_e| = |E|$, while $|\mathcal{X}| = 2\,|F|$. As such, the differential operators are also different in dimensions.

Note that the commonly used diagonal M_1 is a lumped version of the "correct" (Galerkin) mass matrix for 1-forms, integrating over the interpolated 1-Whitney forms. The reason for using the lumped version is that diagonal matrices are comfortable to work with, especially with regards to solving equations. Nevertheless, interpolated closed (and a subgroup, exact) 1-forms are piecewise-constant; in that case, M_1 is the exact inner product for closed forms in $\mathcal{Z}_1$. This is ultimately the reason why the FEM and DEC Laplacians identify.

We summarize the set of differential operators for both FEM and DEC in Table 1.

DEC has an advantage over FEM in the sense that it allows for a natural separation between the combinatorial differential operators d, and the metric induced by the mass matrices, whereas PCVF spaces do not exhibit this separation. This distinction plays an important part in our definition of the subdivision operators. However, there is no existing definition for DEC that allows the full generality of N-directional fields that FEM admits.

4 SUBDIVISION EXTERIOR CALCULUS

Subdivision surfaces. A subdivision surface is a hierarchy of refined meshes, starting from a coarse *control mesh*, and converging into a smooth fine mesh. In this paper, we focus on approximative triangle mesh schemes for both vertex-based functions and face-based functions. Extending notation from [de Goes et al. 2016b; Wang et al. 2006], we denote a subdivision operator as $S^l_{\mathcal{P}}$, where it subdivides an object of space $\mathcal{P}$, and from a mesh in level l, denoted as $\mathcal{M}^l$, to an element of the refined space in $\mathcal{M}^{l+1}$. For instance, $S^5_{\mathcal{E}^*}$ subdivides a non-oriented integrated edge quantity from level 5 to level 6.

We denote the product of subdivision matrices from the coarsest level to a given level l as: $\mathbb{S}^l_{\mathcal{P}} = \prod_{i=0}^{l} S^i_{\mathcal{P}}$. The columns of $\mathbb{S}^l_{\mathcal{P}}$ converge into refined basis functions $\Psi^0_{\mathcal{P}}$ defined on M^0. These basis functions admit a nested refinable heirarchy:

$$\Psi^0_{\mathcal{P}} \subset \Psi^1_{\mathcal{P}} \subset \cdots \subset \Psi^l_{\mathcal{P}}, \tag{8}$$

where a function $\Psi^l_{\mathcal{P}}$ at level l is a linear combination of basis functions at level $\Psi^{l+1}_{\mathcal{P}}$, and where the linear combination coefficients are encoded in the matrix $S^l_{\mathcal{P}}$, as $\Psi^l_{\mathcal{P}} = \Psi^{l+1}_{\mathcal{P}} S^l_{\mathcal{P}}$.

Structure-preserving subdivision. The essence of Subdivision Exterior Calculus (**SEC**) is the definition of stationary subdivision matrices for k-forms that commute with differential operators as follows:

$$\begin{aligned} d_0 S_0 &= S_1 d_0, \\ d_1 S_1 &= S_2 d_1. \end{aligned} \tag{9}$$

This commutation reproduces both exact and curl-free under subdivision. In the more general case, the curl of the subdivided field is the subdivided curl of the coarse field. The divergence also has a predictable behaviour, as we see in the following.

Coarse-to-fine inner products. Choosing Loop subdivision [Loop 1987] for S_0 and halfbox spline subdivision [Prautzsch et al. 2002] for S_2 completely defines S_1 in terms of the Loop and halfbox spline subdivision parameter, assuming symmetry and a fixed odd stencil. In [de Goes et al. 2016b], the subdivision operator is mainly used for the purpose of replacing coarse mass matrices with *restricted* fine mass matrices (alternatively, as a multigrid preconditioner):

$$\mathbb{M}_k = \left(\mathbb{S}^l_k\right)^T \cdot M^l_k \cdot \mathbb{S}^l_k. \tag{10}$$

The restricted mass matrix $\mathbb{M}^0_k$ is exactly the product between subdivided k-forms in the fine level l, which is a parameter that controls the depth of the hierarchy. The restricted mass matrices are in general no longer diagonal; however, they have a limited support (usually just two rings), inherited from the support of the subdivision matrix. As preconditioners, they improve the differential operators for which they are building blocks. This is the case since stationary subdivision operators, as uniform averaging operators, improve the quality of the mesh in the finer levels.

The SEC divergence operator then has the following formulation:

$$\begin{aligned}\left(d_0\right)^T \mathbb{M}_1 z_1^0 &= \left(d_0\right)^T \left(\mathbb{S}_1^l\right)^T \cdot M_1^l \cdot \mathbb{S}_1^l z_1^0 \\ &= \left(\mathbb{S}_1^l\right)^T \left(d_1\right)^T \cdot M_1^l \cdot \left(\mathbb{S}_1^l z_1^0\right) \\ &= \left(\mathbb{S}_1^l\right)^T \left(\left(d_1\right)^T \cdot M_1^l \cdot z_1^l\right) \\ &.\end{aligned} \tag{11}$$

In words, the SEC divergence of a coarse 1-form z_0^1 subdivided into fine 1-form z_1^l is not exactly the subdivided coarse divergence; it is rather equal when integrated under the *test functions* in the columns of $\mathbb{S}_1^l$. Simply put, the divergence of the fine form might contain "high-frequency" components that are in $ker\mathbb{S}_1^l$, but they cancel out under integration with the smooth functions in the columns of $\mathbb{S}_1^l$ to the coarse divergence, effectively like a low-pass filter.

The framework of SEC does not trivially extend to FEM; this is because FEM operators do not factor into combinatorial and metric components, and thus creating stationary subdivision matrices for PCVFs is a challenging task. Our goal is then to create a framework of commutation and hierarchy of spaces for FEM piecewise-constant directional fields. For this, we need to first overcome the challenge of metric-free representation that allows commutation. We do so in the next section.

4. Halfedge forms

For each oriented edge e_{ik} adjacent to faces f and g, we consider its *halfedges* $e_{ik,f}$ and $e_{ik,g}$. Note that they are both oriented in the same direction as e_{ik}; this is departing from the usual doubly-connected edge list convention [de Berg et al. 2008], where halfedges are of opposing orientations, and positively oriented towards their respective face. We choose to co-orient them with the edge as it is a more natural convention for our differential operators.

We define Γ as the space of *null-sum* oriented scalar quantities on halfedges: for every face t with halfedges e_1, e_2, e_3, and with signs s_1, s_2, s_3 that encode the orientation of the respective edges with regards to t (see Section 3), we consider corresponding scalar quantities $\gamma_{1,t}, \gamma_{2,t}, \gamma_{3,t}$ that must hold:

$$s_1\gamma_{1,t} + s_2\gamma_{2,t} + s_3\gamma_{3,t} = 0. \tag{12}$$

We denote $\gamma = \left\{\gamma_{e,t}\right\} \in \Gamma$ as a *halfedge form*.

Equivalence to $\mathcal{X}$. Consider the operator $P' : \mathcal{X} \to \Gamma$, defined as follows:

$$P'_{|t} = \begin{pmatrix} s_1 e_1 \\ s_1 e_2 \\ s_3 e_3 \end{pmatrix}. \tag{13}$$

Note that $P'_{|t}$ has zero row sum, as the sum of edges of a single triangle oriented with the proper signs; its null space is spanned by the normal to the triangle. For each $v \in \chi$, the null sum of $\gamma = P'v$ is trivially satisfied. The operator P' is similar in spirit to the "#" operator in DEC that converts a 1-form to a vector field using metric.

Conversely, for every $\gamma \in \Gamma$, which has null sum by definition, the system $P'v = \gamma$ has a single solution that is also a tangent vector (without normal components)—it can be reproduced by the Penrose-Moore pseudo-inverse $v = P^{-1}\gamma$ (similar to the DEC "♭" operator). This creates a bijection between the spaces Γ and $\mathcal{X}$, and they are therefore isomorphic. We note that we are not aware of this construction made explicitly to represent PCVFs in the literature; a similar construction is alluded to in [Poelke and Polthier 2016].

Representation in practice. In order to naturally enforce a null sum, for each face we only keep the first two γ values: $\gamma_{1,t}$ and $\gamma_{2,t}$. Note that this is done without loss of generality (the choice can be arbitrary). To work with all three when needed, we define an *extension* operator Q that reconstructs $\gamma_{3,t}$, so that:

$$Q_{|t}\begin{pmatrix} \gamma_{1,t} \\ \gamma_{2,t} \end{pmatrix} = \begin{pmatrix} \gamma_{1,t} \\ \gamma_{2,t} \\ s_3\left(-s_{1,t}\gamma_{1,t} - s_{2,t}\gamma_{2,t}\right) \end{pmatrix}$$

This representation "costs" 2 scalars per triangle, which is exactly the dimension of the space of PCVFs, so we do not have to deal with any normal fibrations. The operator Q^{-1} (pseudo-inverse) simply throws away $\gamma_{3,t}$ if the null-sum condition is met, and otherwise filters out any existing sum. With this representation, we reduce P' to the actual operator we use, P, and then its pseudo-inverse P^{-1} is an actual inverse, where we get:

$$P_{|t} = \begin{pmatrix} s_1 e_1 \\ s_2 e_2 \end{pmatrix}. \tag{14}$$

$$P^{-1}_{|t} = \frac{1}{2A_t}\begin{pmatrix} -s_2 e_2^{\perp} \\ s_1 e_1^{\perp} \end{pmatrix}^T$$

P and P^{-1} aggregate the per-face matrices into global operators. Note that $s_1 e_1 \cdot -s_2 e_2^{\perp} = |e_1 \times e_2| = 2A_t$. As such, we have $P \cdot P^{-1} = I_{2\times 2}$ and $P^{-1} \cdot P$ is the 3×3 matrix that projects out the normal component from an ambient vector field on the faces.

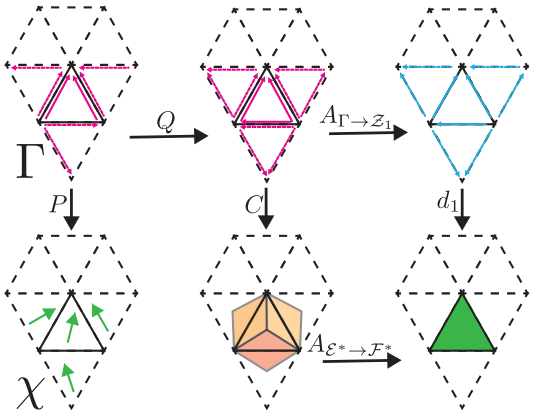

Fig. 3. The FEM operators in Halfedge-form representation.

1 HALFEDGE DIFFERENTIAL OPERATORS

We next redefine all differential operators for Γ with the underlying paradigm that they should be equivalent to the operators in χ, except formulated in Γ terms. We summarize these operators in Figure 3.

Conforming gradient. Consider the assignment operator $A_{\mathcal{Z}_1\to\Gamma}$ that creates a halfedge form from a 1-form by copying the associated single scalar on an edge to its two halfedges. Then, we have that:

$$P^{-1}\cdot Q^{-1}\cdot A_{\mathcal{E}\to\Gamma}\cdot d_0 f = G_{\mathcal{V}} f. \tag{15}$$

The above relation demonstrates how DEC aligns with Γ where exact 1-forms, lended to halfedge forms, represent gradient fields—a fundamental parallel relation between DEC and $\mathcal{X}$ (which directly leads to the equivalence of the Laplacians). To avoid cumbersome notation, we denote $d_{0,\Gamma} = Q^{-1}\cdot A_{\mathcal{Z}_1\to\Gamma}\cdot d_0$, which is the gradient operator in Γ space.

We define $d_{1,\Gamma}$ to be the (oriented) sum operator $d_{1|t} = \sum_{i=1}^{3} s_{i,t}\gamma_{i,t}$ (working similar to DEC d_1, except with the halfedges of the face rather than 1-forms). Note that we always get $d_1\gamma = 0$ for every $\gamma\in\Gamma$, as they must have a null sum.

Note that the transpose operator $\left(A_{\mathcal{Z}_1\to\Gamma}\right)^T = A_{\Gamma\to\mathcal{Z}_1}$ results in 1-forms by summing up the scalars of halfedges into their associated edges; we use it extensively in Section 3.

Curl. The curl operator $C:\Gamma\to\mathcal{E}^*$ is readily defined in Γ space as:

$$C_{\Gamma|ik} = \gamma_{ik,ijk} - \gamma_{ik,kli}. \tag{16}$$

As such, curl-free fields in Γ (or the equivalent χ) are evidently such that the halfedge forms identify on both sides of the edge, which means they are isomorphic to 1-forms. As the null-sum constraint also dictates $d_{1,\Gamma}\gamma = 0$ by definition, we have have that a curl-free γ is isomorphic to a closed 1-form. However, a halfedge form that is not curl free is not compatible with any DEC quantity. Note that we have $C\cdot d_{0,\Gamma} = 0$, which preserves the exact sequence of χ.

2 INNER PRODUCT

As the space Γ represents vectors in χ, the inner product between two halfedge forms $\gamma_1,\gamma_2\in\Gamma$ is consequently defined as:

$$\left(P^{-1}\gamma_1\right)^T M_{\mathcal{F}}\left(P^{-1}\gamma_2\right) = \gamma_1^T\left(P^{-T}M_{\mathcal{F}}P^{-1}\right)\gamma_2 = \gamma_1^T M_\Gamma\gamma_2. \tag{17}$$

M_Γ has the following simple structure:

$$M_{\Gamma|t} = \frac{1}{2}\left(Q_{|t}\right)^T\begin{pmatrix} cot\alpha_1 & & \\ & cot\alpha_2 & \\ & & cot\alpha_3\end{pmatrix}Q_{|t}, \tag{18}$$

where α_j is the angle opposite edge j in face t with our usual notation, and Q is the extension operator as before. Simply put, we get a diagonal mass matrix for the complete null-summed $\gamma\in\Gamma$. We show the proof in Appendix A.

Divergence and Laplacian. Equipped with the inner product, the (conforming) divergence is define as:

$$D_\Gamma = \left(d_{0,\Gamma}\right)^T M_\Gamma. \tag{19}$$

The (integrated) Laplacian is then:

$$L_\Gamma : \mathcal{V} \to \mathcal{V}^* := \left(d_{0,\Gamma}\right)^T \cdot M_\Gamma \cdot d_{0,\Gamma}, \tag{20}$$

which is exactly the cotangent Laplacian, as expected, since Γ represents χ.

We summarize the entire set of differential operators for χ in the Γ setting in Table 1, contrasting them with the analogous DEC and FEM operators.

Operator	**FEM**		**DEC**		Γ	
	Spaces	**formulation**	**Spaces**	**formulation**	**Spaces**	**formulation**
Primal gradient	$\mathcal{V} \to \chi$	$G_\mathcal{V}$	$\mathcal{V} \to \mathcal{Z}_1$	d_0	$\mathcal{V} \to \Gamma$	$d_{0,\Gamma} = Q^{-1} A_{\mathcal{Z}_1 \to \Gamma} d_0$
Dual rotated gradient	$\mathcal{E} \to \chi$	$JG_\mathcal{E}$	$\mathcal{F}^* \to \mathcal{Z}_1$	$M_1^{-1} d_1^T$	$\mathcal{E} \to \Gamma$	$M_\Gamma^{-1} C_\Gamma^T$
Divergence	$\chi \to \mathcal{V}^*$	$G_\mathcal{V}^T M_\mathcal{F}$	$\mathcal{Z}_1 \to \mathcal{V}^*$	$d_0^T M_1$	$\Gamma \to \mathcal{V}^*$	$D_\Gamma = \left(d_{0,\Gamma}\right)^T M_\Gamma$
Curl	$\chi \to \mathcal{E}^*$	$G_\mathcal{E}^{*T} M_\mathcal{F}$	$\mathcal{Z}_1 \to \mathcal{F}^*$	d_1	$\Gamma \to \mathcal{V}^*$	$C_\Gamma = QC$
Primal Laplacian	$\mathcal{V} \to \mathcal{V}^*$	$G_\mathcal{V}^T M_\mathcal{F} G_\mathcal{V}$	$\mathcal{V} \to \mathcal{V}^*$	$d_0^T M_1 d_0$	$\mathcal{V} \to \mathcal{V}^*$	$\left(d_{0,\Gamma}\right)^T M_\Gamma d_{0,\Gamma}$
Dual Laplacian	$\mathcal{E} \to \mathcal{E}^*$	$JG_\mathcal{E}{}^T M_\mathcal{F} JG_\mathcal{E}$	$\mathcal{E} \to \mathcal{E}^*$	$d_1 M_1^{-1} d_1^T$	$\mathcal{E} \to \mathcal{E}^*$	$C_\Gamma M_\Gamma^{-1} \left(C_\Gamma\right)^T$
Hodge Laplacian	$\chi \to \chi$	$G_\mathcal{V} M_\mathcal{V}^{-1} G_\mathcal{V}^T M_\mathcal{F} +$ $JG_\mathcal{E} M_\mathcal{E}^{-1} JG_\mathcal{E}{}^T M_\mathcal{F}$	$\mathcal{Z}_1 \to \mathcal{Z}_1$	$d_0 M_\mathcal{V}^{-1} d_0^T M_1 +$ $M_1^{-1} d_1^T M_\mathcal{F}^{-1} d_1$	$\Gamma \to \Gamma$	$d_{0,\Gamma} M_\mathcal{V}^{-1} \left(d_{0,\Gamma}\right)^T \cdot M_\Gamma +$ $M_\Gamma^{-1} \left(C_\Gamma\right)^T M_\mathcal{E}^{-1} C_\Gamma$

Table 1. Operators per representations. All operator are presented in their integrated versions when applicable.

3 MEAN-CURL REPRESENTATION

While the halfedge forms $\gamma \in \Gamma$ have a simple connection, via the projection operators P and P^{-1}, to the equivalent PCVFs in $\mathcal{F}$, we need an alternative and equivalent representation for them that reveals their differential properties, to be used in our subdivision schemes. Given the two halfedge forms $\gamma_{ik,1}$ and $\gamma_{ik,2}$ on both sides of edge ik adjacent to triangles t_1 and t_2 in our usual notation, we define

$$\begin{aligned} a_{ik} &= \frac{\gamma_{ik,1} + \gamma_{ik,2}}{2} \Rightarrow a = \frac{1}{2} A_{\Gamma \to \mathcal{Z}_1} \cdot Q\gamma \\ c_{ik} &= \frac{\gamma_{ik,1} - \gamma_{ik,2}}{2}. \Rightarrow a = \frac{1}{2} C_\Gamma \cdot \gamma \end{aligned} \tag{21}$$

In words, a_{ik} is the mean of the two halfedge forms, and c_{ik} is half of the curl for the equivalent $\gamma \in \Gamma$. This alternative representation has the following advantages:

- The curl is represented explicitly, allowing for a direct application of the required commutation rule.
- $c_{ik} = 0$ for curl-free fields, and consequently a_{ik} is exactly the associated closed 1-form in DEC.

Note that a_{ik} is an oriented quantity, and hence a 1-form in $\mathcal{Z}_1$, but c_{ik} is a non-oriented integrated quantity in $\mathcal{E}^*$. We emphasize that a_{ik} is *not* in general curl-free in the DEC sense $d_1 a = 0$; the only exception is when the equivalent vector field in $\mathcal{X}$ is curl-free. The conversion back to Γ can be written as:

$$\gamma = Q^{-1} \left(A_{\mathcal{Z}_1 \to \Gamma}\right)^T a - C^T c.$$

Null sum constraint. The mean-curl representation is not trivially equivalent to Γ, since it has values for all edges, whereas γ is represented on two halfedges within each triangle (hence the use of Q^{-1}). For equivalence, we need to hold the null-sum requirement on a and c. It has a surprisingly elegant form; consider again a face ijk, and the respective signs s for the adjacent halfedge forms γ. Then:

$$d_{1,\Gamma} \cdot \gamma = 0 = s_{ij}\gamma_{ij} + s_{jk}\gamma_{jk} + s_{ki}\gamma_{ki} = \tag{22}$$
$$s_{ij}a_{ij} + s_{jk}a_{jk} + s_{ki}a_{ki} - c_{ij} - c_{jk} - c_{ki} =$$
$$d_{1|f}a_f - A_{\mathcal{E}^* \to \mathcal{F}}c_f$$

where $d_{1|f}$ is the DEC d_1 operator restricted to f, and $A_{\mathcal{E}^* \to \mathcal{F}}$ is the summation operator $c_{ij} + c_{jk} + c_{ki}$ (similar to $A_{\Gamma \to \mathcal{E}}$). Note again that when c_f is 0, we just get the DEC $d^2 = 0$. More generally, the DEC definition of curl (see table 1) is exactly $d_1 a$; as such, the DEC face-based curl of the averaged 1-form a is then exactly the summed edge-based FEM curl of the underlying field γ. We are not aware of this connection between DEC curl and FEM curl ever pointed out.

The mean-curl representation reveals other ties between DEC and FEM more clearly:

- γ is FEM-exact if and only if "a" (as a 1-form) is DEC-exact with the same function $f \in \mathcal{V}$.
- γ is FEM-harmonic if and only if "a" is DEC-harmonic.
- Suppose that γ is FEM-co-exact. There exists some $g \in \mathcal{E}^*$ such that $P^{-1}Q\gamma = JG^*g$. Then, we have $c = L_{\mathcal{E}}g$, and a is fully determined from c, as the unique 1-form that holds the following two conditions:

$$D_\Gamma \gamma = D_\Gamma Q^{-1}\left(\left(A_{\mathcal{Z}_1 \to \Gamma}\right)^T a - C^T c\right) = 0 \Rightarrow \tag{23}$$
$$d_0^T M_1 a = D_\Gamma C^T c,$$
$$d_1 a = A_{\mathcal{E} \to \mathcal{F}} c \tag{24}$$

To summarize, harmonic and exact spaces are equivalent in FEM and DEC. Co-exact space are not the same, since they have different dimensionality. However, the DEC-curl of the averaged 1-form of some FEM field is just the average of the FEM-curl.

4 DISCUSSION: REFINABLE HODGE DECOMPOSITION

Given the insights of the mean-curl representation, there is a subtle, yet important, distinction between the way DEC and FEM treat the Hodge decomposition, which we need to make in order to properly define subdivision for PCVF. The DEC hodge decomposition decomposes a 1-form $z_1 \in \mathcal{Z}_1$ into pointwise $z_0 \in \mathcal{V}$, harmonic part z_h, and *integrated* $z_2 \in F^*$. They further rely on refinable function spaces to perform subdivision (Section 4). For this, using integrated F^* is the correct choice (note that SEC subdivides the curl $c = L_2 z_2$ rather than z_2 itself), since it is refinable. The pointwise dual 2-forms are not generally refinable and using them in this manner is a sort of "variational crime".

However, the FEM hodge decomposition uses the pointwise $g \in \mathcal{E}$ for its co-exact part, which is, analogously to the dual 2-form space z_2^*, not refinable. However, our subdivision works on the refinable curl in $\mathcal{E}^*$. Moreover, the hodge decomposition can be defined directly by using f, c, and h as following:

$$\forall \gamma \in \Gamma,\ \exists f \in \mathcal{V},\ c \in \mathcal{E}^*,\ h \in H_\Gamma,\ \gamma = d_{0,\gamma} f + M_\Gamma^{-1} C_\Gamma^T L_{\mathcal{E}}^{-1} c + h.$$

Other than revealing algebraic relations between FEM and DEC, the advantage of the halfedge representation, and moreover in its mean-curl form, is useful to create PCVF subdivision schemes, as we see in the next section.

5. Subdivision vector fields

Our purpose in constructing subdivision schemes for halfedge forms is the ability to work with PCVF in a multi-resolution structure-preserving manner. We define $S_{\mathcal{V}}$ as the Loop subdivision matrix for vertex-based quantities, $S_{\mathcal{F}}$ for the half box spline face-based subdivision matrix, equivalent to S_0 and S_2 in the SEC scheme, respectively. For halfedge-based subdivision, we consider and construct three distinct and interrelated operators:

- S_1, the subdivision matrix for 1-forms.
- $S_{\mathcal{E}^*}$, a subdivision matrix for non-oriented integrated edge-based quantities.
- S_Γ, a subdivision matrix for halfedge forms composed of both.

The first subdivision matrix is defined in SEC, so our purpose is do define the latter two. We note that for clarity, we often omit the level notation l, as the operators are stationary, and the level can be understood from the context.

In order to enable multi-resolution directional field design, we require that S_Γ and $S_{\mathcal{E}^*}$ obey the following commutation rules:

$$\begin{aligned} Q \cdot d_{0,\Gamma} \cdot S_{\mathcal{V}} &= S_\Gamma \cdot d_{0,\Gamma} \\ C_\Gamma \cdot S_\Gamma &= S_{\mathcal{E}^*} \cdot C\Gamma. \end{aligned} \tag{25}$$

In words, subdivided halfedge forms that represent gradient fields should result in gradient fields of the subdivided vertex-based scalar function, and the curl of a subdivided vector field should be like the subdivided curl of a vector field. To achieve these conditions, our subdivision matrix for halfedge-forms works on the mean-curl representation as follows:

$$S_\Gamma \cdot \gamma = \begin{pmatrix} S_1 & 0 \\ 0 & S_{\mathcal{E}^*} \end{pmatrix} \begin{pmatrix} a \\ c \end{pmatrix}, \tag{26}$$

Since S_Γ is defined on the unpacked mean-curl representation, we need to require that the null-sum condition in this rerpresentation is preserved under subdivision. That is,

$$\gamma \in \Gamma \Rightarrow s_\Gamma \cdot \gamma \in \Gamma \tag{27}$$

We need to define $S_{\mathcal{E}^*}$ so that the commutation and null-sum conditions should hold. For this, we make it adhere to the following additional commutation relation:

$$S_{\mathcal{F}^*} A_{\mathcal{E}^* \to \mathcal{F}^*} = A_{\mathcal{E}^* \to \mathcal{F}^*} S_{\mathcal{E}^*}, \tag{28}$$

where $S_{\mathcal{F}^*} = S_2$ is the halfbox spline 2-form subdivision matrix from SEC. In words, the face-based average of the subdivided curl should be equal to the subdivided average of a curl. This serves two purposes:

(1) The relation elegantly preserves the null-sum requirement, as for level l mean a^l and curl c^l we get:

$$\begin{aligned} \textit{(Level } l \textit{ null-sum constraint)} \quad & d_1 a^l - A_{\mathcal{E}^* \to \mathcal{F}^*} c^l = 0 \Rightarrow \\ \textit{(Subdivision)} \quad & S_{\mathcal{F}^*} d_1 a^l - S_{\mathcal{F}^*} A_{\mathcal{E}^* \to \mathcal{F}^*} c^l = 0 \Rightarrow \\ \textit{(Commutation)} \quad & d_1 S_1 a^l - A_{\mathcal{E}^* \to \mathcal{F}^*} S_{\mathcal{E}^*} c^l = 0 \Rightarrow \\ \textit{(Level } l+1 \textit{ null-sum constraint)} \quad & d_1 a^{l+1} - A_{\mathcal{E}^* \to \mathcal{F}^*} c^{l+1} = 0. \end{aligned} \tag{29}$$

and we get that null-sum is preserved in level $l+1$ if it is preserved in level l.

(2) Due to the linear commutation relation, we conjecture that $S_{\mathcal{E}^*}$ converges to a smooth curl in the same order of smoothness and of convergence as $S_{\mathcal{F}^*}$.

We give the exact templates for both S_1 (the same as in [de Goes et al. 2016b] for completeness) and $S_{\mathcal{E}^*}$ in Appendix B. We show an example of a basis function of the subdivision operator in Figure 4, and some examples of full subdivision vector fields in Figure 5.

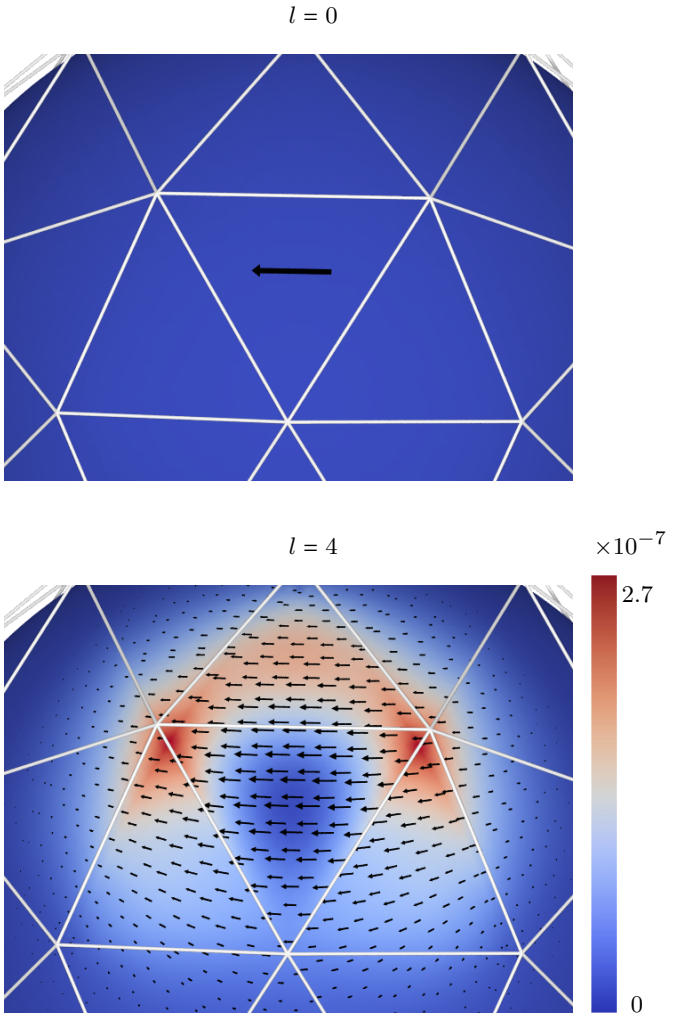

Fig. 4. Basis function for a single vector on a curved domain with positive curvature for coarse ($l = 0$) and fine level ($l = 4$). The initial vector is of unit length. The colorcoding on the fine level depicts the local Hodge energy ($C_\Gamma^2 + D_\Gamma^2$ of the γ-field, represented on vertices for visualization). The glyph arrows on the fine level visualize direction and relative magnitude compared to the other values.

1 BOUNDARY BEHAVIOR

Our concepts of halfedges and the differential operators do not extend trivially to the boundary. Recall that our reasoning for subdivision is to commute with the gradient and the curl operators. However, the discrete curl operator on the boundary is not well-defined for a single edge: consider a boundary face f where the adjacent boundary edge is e_{ij} (see inset), and the halfedge form on that edge is γ_{ij}. As studied in [Poelke and Polthier 2016], the Hodge decomposition of meshes with boundaries admit several valid choices for decomposition, culminating in either Dirichlet of Neumann boundary conditions. We choose to assume to commute with the gradient of a function defined everywhere, including the boundary, and that the boundary curl is consequently zero. That is, on the boundary, we use $a_{ij} = \gamma_{ij}$ and $c_{ij} = 0$. Our subdivision matrices are consequently defined, where $S_{\mathcal{E}^*}$ reproduces zero curl on the boundary, and S_1 is redefined to preserve the null-sum with this constrained $S_{\mathcal{E}^*}$. We show an illustration of basis functions on the boundary in Figure 6.

2 SEM DIFFERENTIAL OPERATORS

Following the reasoning of Section 4, we can modify M_Γ as follows:

$$\mathbb{M}_\Gamma^0 = \left(\mathbb{S}_\Gamma^l\right)^T \cdot M_\Gamma^l \cdot \mathbb{S}_\Gamma^l, \tag{30}$$

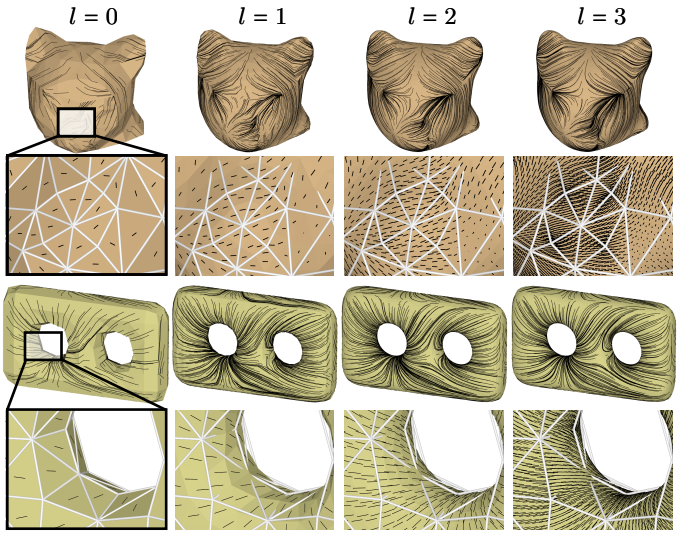

Fig. 5. Multiple levels of subdivided fields on the bitorus (genus = 2) and cathead (genus = 0) models. Per model, the toprow shows the streamlines of the vectorfield. Below, a zoom in is given depicting the local behaviour of the subdivision.

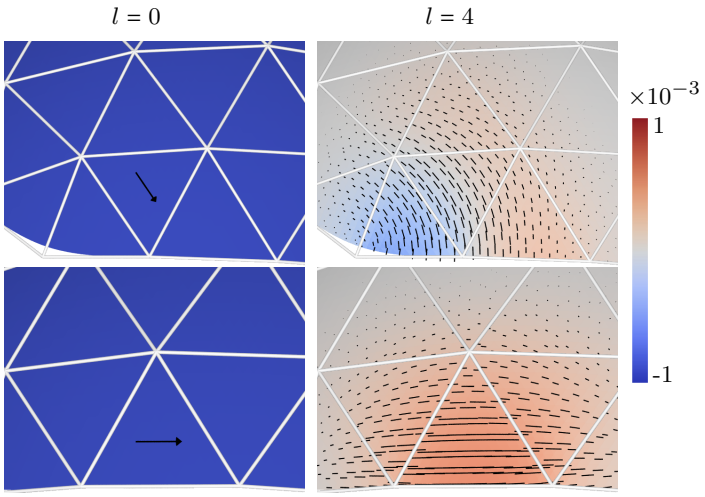

Fig. 6. Basis functions on curved domain with positive curvature for coarse and fine level near the boundary. The initial vector is of unit length. The colorcoding depicts the local face averaged curl.

and consequently replace every instance of M_Γ^0 with $\mathbb{M}_\Gamma^0$ in Table 1, to get the new version of the differential operators. We will denote these operations as **SEM**'ed operators (SEM being *Subdivision Element Method*, in analogy with SEC's *Subdivision Exterior Calculus*). By the commutation relations, it is straightforward that fields that are processed with SEM have the same structure-preserving property, with regards to exactness and curl, as those in FEM due to the commutation relations. However, for the divergence of a coarse field γ^0, upon subdivision to a fine field $\gamma^l = \mathbb{S}_\Gamma^l \gamma^0$, we get

$$\begin{aligned} \mathbb{D}^0\gamma^0 = d_{0,\Gamma}^T \mathbb{M}_\Gamma^0 \gamma^0 = \\ d_{0,\Gamma}^T \left(\mathbb{S}_\Gamma^l\right)^T \cdot M_\Gamma^l \cdot \mathbb{S}_\Gamma^l \gamma^0 = \\ \left(\mathbb{S}_\mathcal{V}^l\right)^T d_{0,\Gamma}^T \cdot M_\Gamma^l \gamma^l = \left(\mathbb{S}_\mathcal{V}^l\right)^T D^l \gamma^l, \end{aligned} \tag{31}$$

similar to the SEC result in Equation 11.

Note that we use $\mathbb{D}$ to denote the SEM divergence operator in line with other notation. In words, the divergence of a subdivided field is equal to the divergence of the resulting coarse field only through the restriction $\mathbb{S}^T$ (alternatively, testing with the coarse trial function). That essentially means that the divergence of the fine field might have "high frequency" components, defined to be in $\ker\mathbb{S}^T$ (see Figure 9). This still leaves the cohomological structure of SEM intact. Note that the restricted mass matrices $\mathbb{M}$ are not diagonal anymore due to the two-ring support of any $\mathbb{S}$. Additionally, some operators are defined with inverse mass matrices, which are dense and non-local. In practice, we almost never need to compute the exact inverse, and we show how circumvent this problem in the relevant applications.

Level	L_∞
0	0.6778e-4
1	0.5431e-4
2	0.5442e-4
3	0.5321e-4
4	0.5315e-4
5	0.5313e-4

Table 2. Operator L_∞ error for the cone model (Figure 8).

2.1 Errors and convergence

To study the behavior of our PCVF subdivision, we look at the behaviour of the SEM Hodge Laplacian for the vector equation:

$$L_\Gamma \cdot \gamma = b,$$

where $b \in \Gamma$ is some given field and L_Γ the Hodge Laplacian. We conduct two tests:

- **Projection error:** we choose b^0 procedurally on some coarse mesh (level 0), and subdivide it to get b^l, where we consider the resulting $\overline{\gamma}^l$ as the ground truth reference. We test the projection error of our SEM operators: the error of using a low-dimensional approximation of the fine function space. For each level $0 \leq k < l$ we compute γ for the SEM Laplacian $\mathbb{L}_\Gamma^k$ and the FEM Laplacian L_Γ^k. Then, we subdivide γ^k to γ^l and measure the L_2 and L_∞ error against the ground truth solution $\overline{\gamma}^l$. We show the results in Figures 7 and 8 for two different meshes. As can be seen, the SEM error is lower than the FEM error and converges to a small error.
- **Operator error:** we perform a similar test, except that we solve everything on the coarse mesh $l = 0$, and modify the level of depth k for the SEM operator. This gives us the operator error, measuring the accuracy of an operator constructed on the coarse level with relation to the fine level. We show the result in Table 2.As can be seen, the operator diminishes with higher subdivision level, but plateaus near the highest subdivision level. This suggests that a reasonable approximation can be accomplished with a fairly low SEM level.

2.2 Hodge decomposition

In Figure 9 we show a Hodge decomposition of a procedurally-created field with the SEM operators, subdivided to a fine level $l = 3$. It is evident that the exact part subdivides by definition, but also that there high-frequency divergence is added to the co-exact and the harmonic part, as demonstrated in Equation 31. We refer to this result as *divergence bleeding*.

2.3 Hodge Spectrum

The spectrum of the Hodge Laplacian L_χ was studied in [Brandt et al. 2016], where they showed that the spectrum of L_χ comprises harmonic fields (eigenvalue 0), gradients of eigenfunctions of $L_\mathcal{V}$, and cogradients of eigenfunctions of $L_\mathcal{E}$. Using the SEM mass matrices, these relations still hold for the Γ Hodge Laplacian $Ł_\Gamma$:

$$\begin{aligned}
&\forall \phi \in \mathcal{V},\ \lambda \in \mathbb{R},\ s.t.\ \mathbb{L}_\mathcal{V}\phi = \lambda \mathbb{M}_\mathcal{V}\phi \Rightarrow \mathbb{L}_\Gamma \cdot d_{0,\Gamma} \cdot \phi = \lambda \mathbb{M}_\Gamma \cdot d_{0,\Gamma} \cdot \phi. \\
&\forall \psi \in \mathcal{E},\ \mu \in \mathbb{R},\ s.t.\ \mathbb{L}_\mathcal{E}\psi = \mu \mathbb{M}_\mathcal{E}\psi \Rightarrow \mathbb{L}_\Gamma \cdot \mathbb{M}_\Gamma^{-1} C_\Gamma^T \cdot \psi = \mu C_\Gamma^T \cdot \psi.
\end{aligned} \tag{32}$$

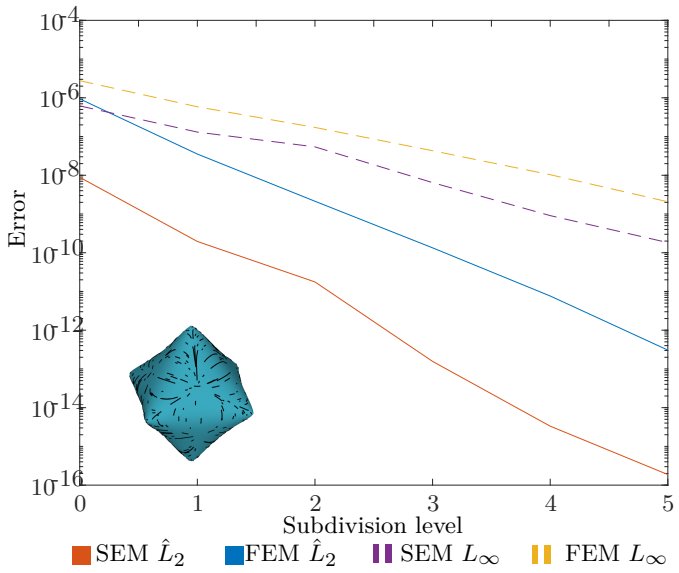

Fig. 7. Log scaled L_∞ and normalized L_2 projection errors for the star model, as a function of subdivision level. The norms are taken over the difference between the fine level solution $\bar{\gamma}^l$ and the soluion at the given subdivision level.

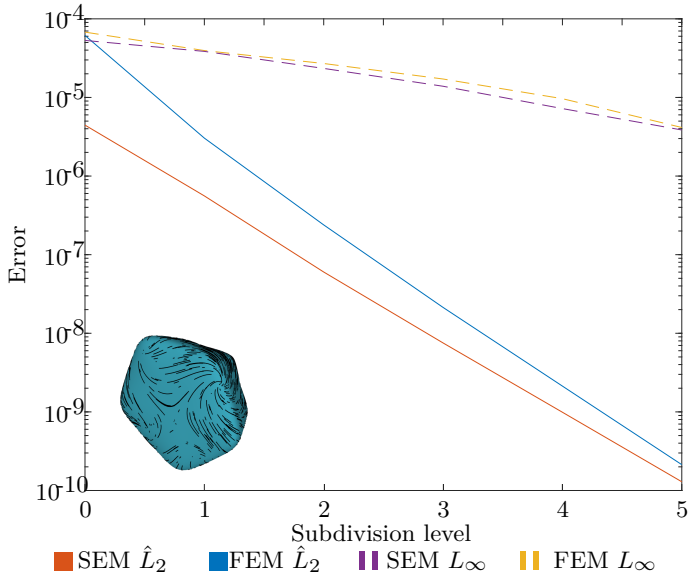

Fig. 8. L_∞ and normalized L_2 projection errors for the cone model, as a function of subdivision level. The norms are taken over the difference between the fine level solution $\bar{\gamma}^l$ and the soluion at the given subdivision level.

Note that a term of $\mathbb{M}_\Gamma \cdot \mathbb{M}_\Gamma^{-1}$ was simplified from the right-hand side of the last equation. We used subdivision level $l = 3$, and computed the SEM Hodge eigenfunctions for several eigenvalues. We compare them against the ground truth fine eigenfunctions in Figures 10 and 11.

In Figures 12 and 13, we also show the fractional difference between the fine eigenvalues and the FEM and SEM eigenvalues for the Hodge Laplacian, where the figures correspond to exact resp. co-exact fields. As can be seen, the SEM eigenvalues remain relatively close to the fine level eigenvalues, even for half the number of eigenfunctions on the given mesh for the conforming Laplacian.

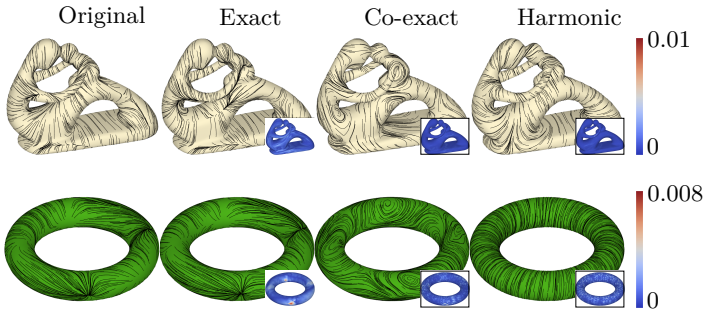

Fig. 9. SEM Hodge decomposition on models with genus 6 and 1 for procedurally generated fields. The streamlines of the initial field and the resulting components of the Hodge decomposition are shown (depicted on the fine level). The insets show the absolute value of the fine level divergence, from which the divergence pollution in the co-exact and harmoninc part at the fine level is evident.

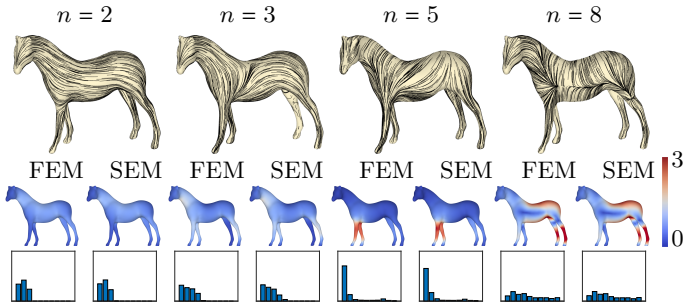

Fig. 10. Eigenfunctions of the Hodge Laplacian that are gradients of the eigenfunctions of the conforming Laplacian. The colorcoding denotes the norm of the pointwise vector difference of the eigenfunctions. Histograms are shown for the fractional amount of differences over the model, scaled from 0 to 1.

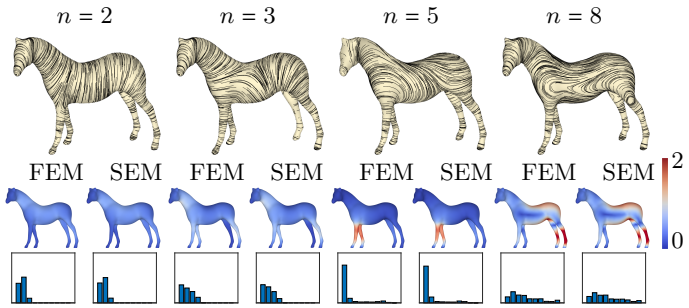

Fig. 11. Eigenfunctions of the Hodge Laplacian that are rotated gradients of the eigenfunctions of the non-conforming Laplacian. The colorcoding denotes the norm of the pointwise vector difference of the eigenfunctions. Histograms are shown for the fractional amount of differences over the model, scaled from 0 to 1.

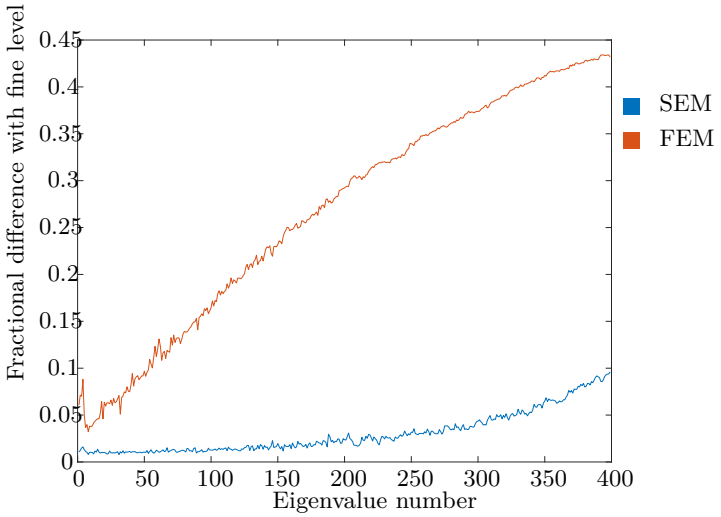

Fig. 12. Fractional difference between the fine level eigenvalues for the conforming Laplacian and the SEM/FEM eigenvalues, calculated as $|\lambda - \lambda_{\text{fine}}|\lambda_{\text{fine}}|$. The mesh has $|V| = 752$

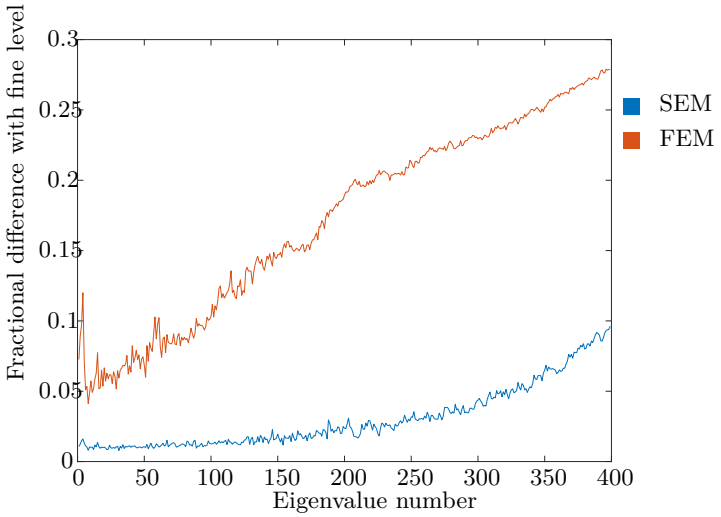

Fig. 13. Fractional difference between the fine level eigenvalues for the non-conforming Laplacian and the SEM/FEM eigenvalues, calculated as $|\mu - \mu_{\text{fine}}|\mu_{\text{fine}}|$. The mesh has $|E| = 2250$.

6. Subdivision N-directional fields

We work with N-directional fields that are elements of χ^N: in each face t there are N indexed vectors $\{v_{t,1}, \ldots, v_{t,N}\}$, not necessarily in any given symmetry. We assume that the field is equipped with a *matching*: a map between the vectors on a face t_1 to the vectors of an adjacent face t_2, and thus associated with the dual edge e between them. We always assume the matching to be (index) *order-preserving*. That is, the matching is parameterized by a single index Ie, where a vector of index k on face t_1 is matched to vector of index $k + Ie$ (modulo N) on face t_2.

The singularity index I_v of a vertex v is defined as $I_v = \frac{1}{N} \sum_{e \in Nv} I_e$ [Vaxman et al. 2016], where Nv is the set of edges attached to vertex v. A regular vertex v has $I_v = 0$; this means that the field on the associated 1-ring can be *combed* (see Figure 14): the field can be re-indexed *locally* in every face of the 1-ring such that $\forall e \in Nv,\ I_e = 0$. With re-indexing, an N-field is locally reduced to N independent fields. A *fractional* singular vertex is defined by having $I_v \notin \mathbb{N}$, where such combing is not possible. Fields with fractional singularities cannot be combed *globally*. This is usually the case, as $\sum_{v \in V} I_v$ is the Euler characteristic of the mesh. *Integral singularities* do not induce matching mismatches, and therefore appear in single-vector fields as well, as sources, sinks, and vortices. They are basically sources of divergence and curl, and are irrelevant to the generalization to directional fields in this section.

1 EXTENDING FEM CALCULUS

To be able to extend our subdivision scheme for N-directional fields, we need a concept of N-halfedge forms, N-scalar functions, and the entire suite of differential operators. For this, we next adapt existing notions from discrete calculus of branching coverings [Bommes et al. 2009; Diamanti et al. 2015; Kälberer et al. 2007]. See Figure 15 for an exemplification of the directional calculus presented here.

Seamless function spaces. Consider a vertex $v \in V$ with adjacent faces (in CCW order) $t_1, \ldots, t_d$, and associated corners $v_1, \ldots, v_d$. Further consider edges e_i between corners v_i and v_{i+1}. The function space $\mathcal{V}^N$ is parameterized by a vector $\mathbf{f}_{v_i}$ of N functions per corner i: $\mathbf{f}_{v_i} = \left(f_{v_1}, \ldots, f_{v_d}\right)^T$. Note: that means $N \cdot d$ values for a single vertex (but as we next see, they are spanned by a lower-dimensional parameter space). The functions are matched across edges in the same way N-directional are: consider two adjacent corners v_i and v_{i+1} across edge e_i with matching index Ie_i. We construct the permutation matrix πe_i that represents the map that the matching induces, and then have:

$$\mathbf{f}_{v_{i+1}} = \pi e_i \cdot \mathbf{f}_{v_i} \tag{33}$$

between the corners of every single face, the function vector just behaves like N separate functions (so there is no matching or translation inside a face).

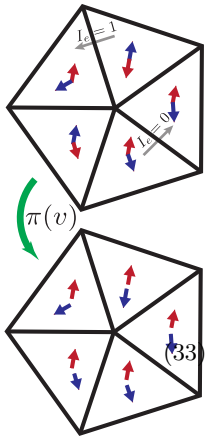

Fig. 14. Matching and combing. Top: a non-singular vertex with two non-zero matching indices. Bottom: since the vertex is non-singular, applying πv results in a combed field where the two fields are separated.

Combing. For regular vertices, and by successively applying Equation 33, we get that $\mathbf{f}_{v_1} = \pi e_d \cdot \mathbf{f}_{v_d}$. As such, we can *comb* the functions over regular vertices, in the same way we do for directional fields: for a single 1-ring, we start from corner v_1 in face t_1, and transform every $\mathbf{f}_{v_i}$ into $\mathbf{f}_{v_1}$ by inverting Equation 33 recursively. We denote this linear transformation as Πv. Note that that means that there are only N independent functions in every regular vertex, parameterized by $\mathbf{f}_{v_1}$, which is expected.

Conforming operators. All the conforming differential operators can be directly extended from the single-vector calculus around regular vertices, by conjugation with the combing (see Figure 15). For instance, we have that the divergence $D^N v : \mathcal{X}^N \to \mathcal{V}^{*N}$ is:

$$D^M = \Pi^{-1} v \begin{pmatrix} d_0^T M_{\mathcal{F}} & & \\ & \ldots & \\ & & d_0^T M_{\mathcal{F}} \end{pmatrix} \Pi v. \tag{34}$$

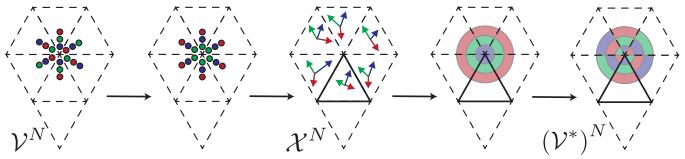

Fig. 15. Example of directional calculus via the directional Laplacian. A vertex based field is combed after which a gradient can be applied due to the matched values. Then, applying the divergence results in a combed integrated value, which has to be combed back for properly representing the operator.

In words, we comb a function and a field around a regular vertex, use the operators on every function in the vector f_{v_1} independently, and then comb back. The result is a vector of N scalars representing the independent divergences of the combed functions. Then, Πv^{-1} combs the N scalars to corner-based values corresponding to original corner indexing.

The gradient operator G_V extends to $G^N_{\mathcal{V}} : \mathcal{V}^N \to \mathcal{X}^N$ by simply operating on the elements in the function vectors of the corners of the face independently, to produce N vectors. Therefore it doesn't require combing; the corners of every single face are always trivially matched to each other. It is important to note that the identity of the "first" corner v_1 does not incur any loss of generality, due to the conjugation; the result per corner would be exactly the same regardless of which corner is first.

Non-conforming operators. Non-conforming differential operators, namely the curl C^N are easier to generalize: we only have to comb two faces, and then conjugate the curl operator independently for the N vectors in both faces with combing as in Equation 33. The result is a function in $\mathcal{E}^{*N}$. The rotated co-gradient $JG^N_{\mathcal{E}}$, exactly like $G^N_{\mathcal{V}}$, is defined per-face and therefore does not require any matching information.

Structure-preserving calculus. It is easy to verify that directional-field calculus is structure-preserving with relation to the exact sequence around regular vertices. We have that $C^N \cdot G^N_{\mathcal{V}} = 0$, and that $D^N \cdot J \cdot G^N_{\mathcal{E}} = 0$ as well. The formal proof is straightforward, given the conjugation of combing and differential operators, and we omit it for brevity. Essentially, the existence of an exact sequence means that we can also define a directional Hodge decomposition, but we leave this line of research for future work.

Around singular vertices. For singular vertices, the product of πe matrices leads to a permutation matrix for the singularity index Iv. That is, "returning" to v_1 after applying Equation 33, we get $\pi v \cdot \mathbf{f}_{v_1} \neq \mathbf{f}_{v_1}$. As such, conforming differential operators are not well-defined for fractional singularities. For this purpose, they can be interpreted as isolated boundary points in the field where there is not enough continuity by definition to allow for conforming operators. The non-conforming operators are well defined everywhere, as they only require two faces in every stencil.

2 EXTENDING Γ^N

Calculus of halfedges is natural in the directional setting. We define $\gamma \in \Gamma^N$ as a vector of N scalars per halfedge. The operators $d^N_{0,\Gamma}$ and $d^N_{1,\Gamma}$ are trivially extended with respect to the matching of the corners. Note that we have a null-sum constraint for each element of γ independently. The same is done for per-face operators $P^N : \mathcal{X}^N \to \Gamma^N$ (and its inverse), extension operator Q^N, and the summation operator $A_{\mathcal{E}^{*N} \to \mathcal{F}^{*N}}$.

The mean-curl representation is defined with the combing, as for nonconforming differential operators like C^N: one of the halfedges in every edge is chosen arbitrarily as the "first", and then we define $A_{\Gamma^N \to \mathcal{Z}^N_1}$ to conjugate with the matching. As such, both the resulting mean "a" and (half) curl c are defined with relation to one of the halfedges, and this choice of "first halfedge" is well-defined up to permutation.

3 EXTENDING SUBDIVISION OPERATORS

Equipped with an extension of the Γ representation to Γ^N, we can next extend our subdivision operators to work with directional fields and preserve their structure.

Branched Loop and half-box splines. For regular vertices, both the Loop $S_{\mathcal{V}}$ and the half-box spline $S^*_{\mathcal{F}}$ subdivision operators extend to the branched spaces $\mathcal{V}^N$ and $\left(\mathcal{F}^*\right)^N$ by conjugation with combing as well. For instance, for Loop subdivision we get:

$$\left(S_{\mathcal{V}}\right)^N = \Pi^{-1} v \begin{pmatrix} S_{\mathcal{V}} & & \\ & \dots & \\ & & S_{\mathcal{V}} \end{pmatrix} \Pi v. \tag{35}$$

The result creates new even and odd edges, where the permutation πe for even edges is the same like the coarse edges they originate from, whereas πe for odd edges is an identity.

For singular vertices, we require a different definition of the subdivision operators. We do so by *unfolding the branch* (see Figure 17): consider again a one ring with d faces, and create a new ring of valence $d \cdot N$ by wrapping around the central vertex v N times. We assign a single scalar function to each face by the order of the matching. We are bound to return to $\mathbf{f}_{v_1}$ since $\pi v^N = I$. We denote the unfolding operation as Φv. Then, we can conjugate $S_{\mathcal{V}}$ for singular vertices with the unfolding:

$$\left(S_{\mathcal{V}}\right)^N = \Phi v^{-1} S_{\mathcal{V}} \Phi v.$$

Note that we use $S_{\mathcal{V}}$ with the valence $d \cdot N$ for the singular vertex.

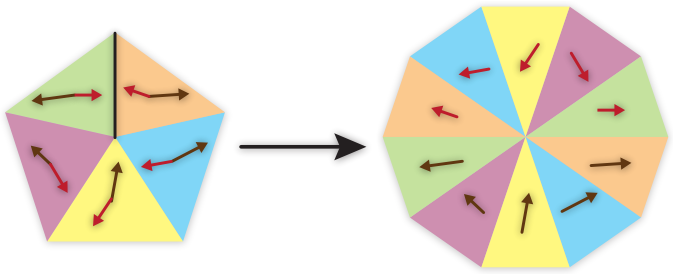

Fig. 16. The unfolding operator Φv, illustrated for a singular vertex in the space $\mathcal{X}^N$. We unfold a valence 6 with $N = 2$ into a valence 12 ring with a single vector field. The vector field will then be locally subdivided with S_Γ and then folded back.

The unfolding Φv is a generalization of the combing operator Πv that allows us to extend all our subdivision operators without altering the original scalar subdivision stencils, as the commutation also works through the conjugation. As a result, we maintain all the differential properties of the subdivision, and among them structure-preserving of curl and exactness. We show the result of our subdivision in Figures 17 and 18.

The number of unique functions that arises via the unfolding operation is determined by the fractional index. For a fractional index I_v of $\frac{i}{N}$, the unfolding generates $\frac{N*i}{\mathrm{LCM}i,N}$ functions, with LCM the least common multiple operation.

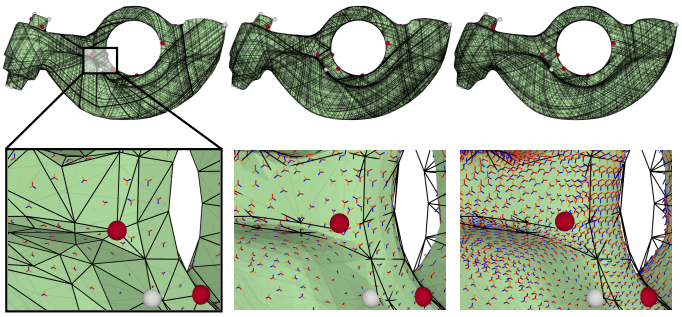

Fig. 17. Streamlines of the coarse level field and subdivisions with $l = 1$ and $l = 2$ for a directional field with $N = 3$. The spheres denote the singularities of the field, with the colors denoting the index: red $= 2/3$, white $= 1/3$. Below, a zoom in is shown around the red singularity

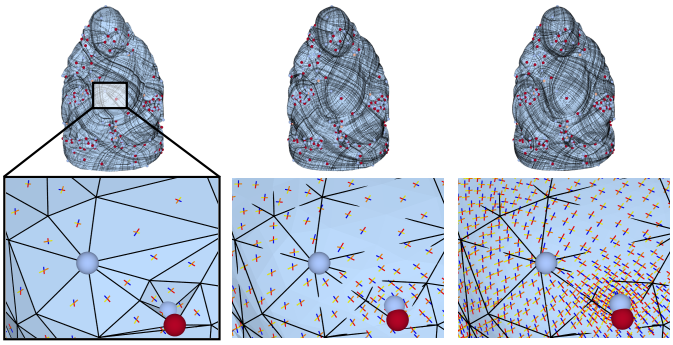

Fig. 18. Streamlines of an as curl free as possible field for the coarse field and the subdivided fields at $l = 1$ and $l = 2$ for $N = 4$. Below, another zoom in is given. Here, the singularities are colored with red $= 3/4$, orange $= 2/4$, white $= 1/4$.

7. Applications

In the following, we apply our SEM framework for several applications that use piecewise-constant directional fields. We implemented the subdivision and the resulting applications using MATLAB, and measured timings on a desktop with an Intel i7-4790 (3.6GHz) CPU and 12 GB of RAM.

1 VECTOR FIELD DESIGN

In Figure 19 we show an example of efficient vector field design. Several vectors are constrained on faces of a coarse mesh, and interpolated to the rest of the mesh by solving for a field γ^0 as follows: $\mathbb{L}^3_\Gamma \gamma^0 = 0$ (using level 3 SEM). We then subdivide to get γ^3 as our result. With this, we get a design for fine fields over the coarse control polygon.

Fig. 19. Vector field design example. The local constraints are shown which are used to perform a constrained minimization of the Dirichlet energy (hard constraints). Shown on fine level $l = 3$ using streamlines.

2 OPTIMAL TRANSPORT

We apply our subdivision to the optimal transport algorithm presented in [Solomon et al. 2014]. For brevity, we do not consider meshes with boundary in this experiment. The formulation computes a geodesic vector field J between two probability distributions $\mu_0, \mu_1 \in \mathcal{V}^*$ so that $_{v\in V}\, \mu_{0|v} = _{v\in V}\, \mu_{1|v} = 1$ defined on the fine mesh of level k. These distributions are controlled by densities $\rho_0 = M_0^{-1}\mu_0 \in \mathcal{V}$ (and similarly for ρ_1). Ultimately, the geodesic field is computed to minimize (a simplification of) the 1-Wasserstein distance $W\mu_0, \mu_1$ between the probability measures as follows:

$$\begin{aligned} W\mu_0, \mu_1 = \inf_{g,h\ t\in F^k} & At \left| G_{\mathcal{V}|t} f + JG_{\mathcal{E}|t} g + h \right|_{L_2} \\ s.t.\ \ & Lf = M_\mathcal{V}\rho_0 - \rho_1. \end{aligned} \tag{36}$$

We have $g \in \mathcal{E}^k$ and h is a harmonic field. $f \in \mathcal{V}$ is totally determined from the Laplacian condition. To limit the solution space on a fine mesh, they use a spectral subspace for g from its Laplacian. We offer an alternative low-rank approximation that uses coarse-mesh function values instead, which is more efficient due to the sparsity of the subdivision matrix. Here, we deviate from the multigrid V-cycle folding paradigm, and solve the problem directly on the fine mesh. Nevertheless, we limit the solution space to subdivided coarse functions. To use the refinable conforming functions, we note that the underlying continuous norm is invariant to J. Therefore, we dualize the discretization of the problem: we consider mid-edge distributions $\rho_0', \rho_1' \in \mathcal{E}^*$, transform the problem to refinable $\gamma \in \Gamma$, and solve for:

$$W\mu_0, \mu_1 = \inf_{f^0, h\, t \in F^k} \sqrt{\gamma_t^T M_\Gamma \gamma_t} \tag{37}$$
$$s.t.\ \gamma = S_\Gamma \left(d_0^\Gamma f^0 \right) + \left(M_\Gamma^k \right)^{-1} C^t g^k + S_\Gamma h^0$$
$$s.t.\ \ L_\mathcal{E} g = M_\mathcal{E} \left(\rho_0' - \rho_1' \right).$$

In words, we solve for coarse f^0 so that its subdivided gradient γ^k, with harmonic components as h, create the least-norm vector field with the Laplacian-computed co-exact component g. This is solved using the ADMM procedure described by [Solomon et al. 2014]. Note that the co-exact component is computed beforehand, and therefore constant after solving the Laplacian equation.

We show our result in Figure 20. For a fair comparison, we use the same amount of fine eigenfunctions (their method) as the number of coarse vertices (in our formulation), so that the problem is solved with the same dimensionality.

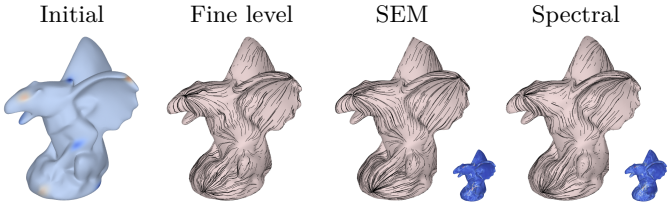

Time	451.2 s	0.6 s	134.8 s
L_2		0.47	0.36
EMD distance	397.4	443.5	400.5

Fig. 20. Comparison of the EMD algorithm between the spectral and SEM approximation. On the left, the inital distribution of masses. The three following figures depict the streamlined J fields resulting from the algorithm, with insets for the spectral and SEM approximations depicting the pointwise difference with respect to the fine level solution. Below, the calculation times are shown. The L_2 difference between the resulting J and the fine level J is given, as well as the calculated Earth Mover's Distance.

3 OPERATOR-BASED ADVECTION

Our framework can be used to modify the operator-based representation of PCVFs introduced in [Azencot et al. 2013, 2015]. Given a vector field $u \in \chi$, their method represents it by offering a discrete version of the classical representation of vector fields as derivations of scalar function f: $\langle v, \nabla f \rangle$. The derivation is discretized as a matrix $B_V : V \times V$ on a mesh as follows:

$$B_V = \frac{1}{3} \left(M_\mathcal{V} \right)^{-1} A_{\mathcal{F} \to \mathcal{V}} M_\mathcal{F} U G_\mathcal{V}, \tag{38}$$

where $U : F \times 3F$ is a matrix that performs the facewise dot-product with u, and $A_{\mathcal{F} \to \mathcal{V}}$ adds values from faces to adjacent vertices, in our usual notation. Essentially, the dot products are made per face, and averaged to the vertices using the respective mass matrices of the mesh.

The operator representation makes it simple to advect a function f on a surface: given time t, and the initial function value $f0$, we have $ft = exptB_V$. Here, an eigenvalue basis is also used to reduce the problem. Define Ψ as the matrix with the Laplacian eigenvectors as columns, then they use:

$$B_V^{EIG} = \Psi^+ B_V \Psi = \Psi^T M_\mathcal{V} B_V \Psi.$$

To make the operator-based approach SEM-compatible, we use the following formulation instead:

$$B_V^{SEM} = S_\mathcal{V}^T B_V S_\mathcal{V},$$

where the U operator is made of a subdivided coarse vector field. We show the result in Figure 21, where the fine operator advection is used as ground truth, and the comparison is with the advected functions subdivided to the fine level. Figure 22 analyzes the error for different eigenvector resolutions. There we see that for the given time range, the SEM solution performs better compared to the <200 eigen functions approximations. For both SEM and the eigenfunctions approximation, the error diverges due to the amplification of the error with respect to the fine level by the exponential operation.

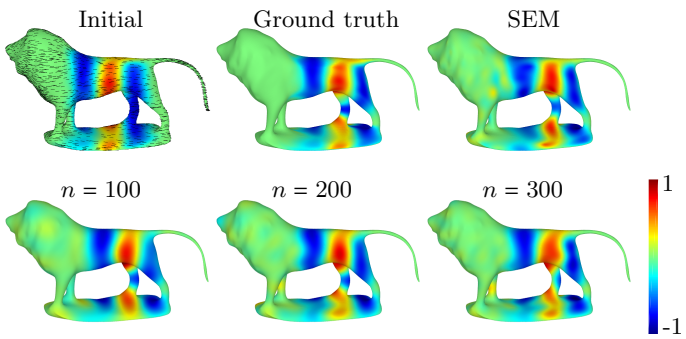

Fig. 21. Advection of results on the lion mesh. The initial field f (colocoding) is advected with the given vector field (glyphs). The groundtruth and SEM result are shown for time $t = 16$. In the row below, results for the same time are shown with the approximation using the first n Laplacian eigenfunctions.

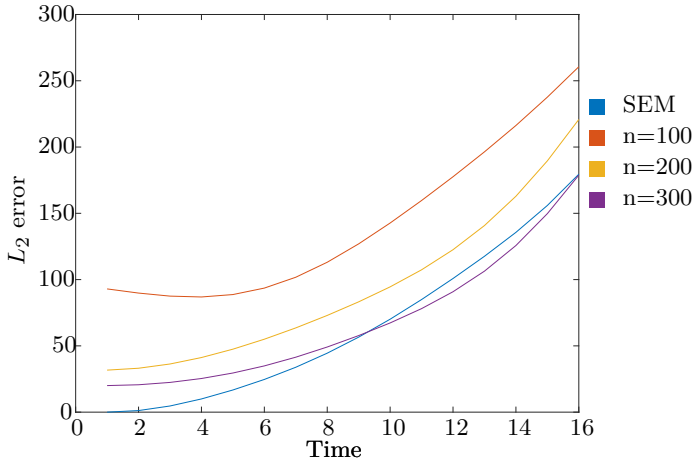

Fig. 22. L_2 error for the SEM and spectral approximations, depicted in Figure 21, compared to the ground truth, for time $t = 1$ to $t = 16$, with stepsize of 1.

8. Discussion

1 CONVERGENCE AND SMOOTHNESS

As we show in the auxiliary material, our subdivision stencils for $S_{\mathcal{E}^*}$ and S_Γ had a few degrees of freedom that we allocated to make the spectrum of the subdivision optimal, such that it converges in the limit since the subdominant eigenvalues are less than 1. However, we leave a formal analysis of smoothness to future work. We conjecture that since the fields are derivatives of smoothly-subdivided functions (and co-functions), they are one level of smoothness lower.

Note that a better practice might be to allow $S_\mathcal{V}$ and $S_{\mathcal{F}^*}$ to vary entirely, where the smoothness of all subdivision operators is optimized concurrently (similar to [Huang and Schröder 2010]).

2 DUAL FORMULATION

Our Γ space is chosen as $\langle v, e\rangle$, but the entire formulation can be done with the perpendicular $\langle v, e^\perp\rangle$, where one should then also use non-conforming divergence and conforming curl. This can be beneficial to simulations of flows.

3 PRECONDITIONING AND ITS DISADVANTAGES

The mass matrices of SEM are generally more strongly positive-definite than those of the FEM in the coarse mesh. The reason is that the uniform and stationary subdivision operators average the mesh, and create better triangulations. Nevertheless, the fact that we do not commute with the original mass matrix also creates the high-frequency divergence pollution in the subdivided fields. It is then worthwhile to try and explore alternatives that consider the mass matrices within the templates, to obtain perfect Hodge decompositions.

4 FULL MULTIRESOLUTION PROCESSING

Our paper explored low-dimensional coarse-to-fine approximations. Moreover, since the basis functions are not orthogonal, the level of approximation is generally worse than of Eigenvectors of the same dimension (expensive as their computation may be). Nevertheless, this method can be augmented with the use of *subdivision wavelets* [Bertram 2004; Lounsbery et al. 1997], to obtain true multi-resolution representation of functions over the fine mesh, with the advantages of increasing locality—this could benefit applications such as solving diffusion problems.

5 NON-TRIANGULAR MESHES

The space χ is not well defined for non-planar quad meshes. Nevertheless, in the spirit of mimetic elements [Bossavit 1998], the space Γ with its null-sum constraint is still well-defined for any possible choice of χ. As such, our framework also extends to polygonal meshes and other subdivision operators (such as Catmull-Clark). We will explore this in future work.

6 GENERAL RESTRICTION OPERATORS

Finally, our setting is currently limited to surfaces made out of subdivision surfaces. It could be beneficial to also allow for a multi-resolution setting on general fine meshes using simplification operators (such as Quadratic-error based simplification [Garland and Heckbert 1997]) as the restriction operators. This should prove challenging as the vertex- and face-based restrictions have to be defined first, but will allow a very general framework for directional-field processing on arbitrary triangle meshes.

REFERENCES

Omri Azencot, Mirela Ben-Chen, Frédéric Chazal, and Maks Ovsjanikov. 2013. An Operator Approach to Tangent Vector Field Processing. *Computer Graphics Forum* 32, 5 (2013).

Omri Azencot, Maks Ovsjanikov, Frédéric Chazal, and Mirela Ben-Chen. 2015. Discrete Derivatives of Vector Fields on Surfaces – An Operator Approach. *ACM Transactions on Graphics* 34, 3 (May 2015).

Ivo Babuška and Manil Suri. 1994. The P and H-P Versions of the Finite Element Method, Basic Principles and Properties. *SIAM Rev.* 36, 4 (Dec. 1994), 578–632. https://doi.org/10.1137/1036141

Mirela Ben-Chen, Adrian Butscher, Justin Solomon, and Leonidas Guibas. 2010. On discrete killing vector fields and patterns on surfaces. *Computer Graphics Forum* 29, 5 (2010).

M. Bertram. 2004. Biorthogonal Loop-subdivision Wavelets. *Computing* 72, 1-2 (April 2004), 29–39. https://doi.org/10.1007/s00607-003-0044-0

Henning Biermann, Adi Levin, and Denis Zorin. 2000. Piecewise Smooth Subdivision Surfaces with Normal Control. In *Proceedings of the 27th Annual Conference on Computer Graphics and Interactive Techniques (SIGGRAPH '00)*. ACM Press/Addison-Wesley Publishing Co., New York, NY, USA, 113–120. https://doi.org/10.1145/344779.344841

David Bommes, Henrik Zimmer, and Leif Kobbelt. 2009. Mixed-integer Quadrangulation. *ACM Transactions on Graphics* 28, 3 (2009).

Alain Bossavit. 1998. In *Computational Electromagnetism*, Alain Bossavit (Ed.). Academic Press, San Diego, 1 – 30. https://doi.org/10.1016/B978-012118710-1/50002-7

Achi Brandt. 1977. Multi-Level Adaptive Solutions to Boundary-Value Problems. *Math. Comp.* 31, 138 (1977), 333–390.

Christopher Brandt, Leonardo Scandolo, Elmar Eisemann, and Klaus Hildebrandt. 2016. Spectral Processing of Tangential Vector Fields. *Computer Graphics Forum* 35 (2016).

Marcel Campen, David Bommes, and Leif Kobbelt. 2015. Quantized Global Parametrization. *ACM Transactions on Graphics* 34, 6 (2015).

Keenan Crane, Fernando de Goes, Mathieu Desbrun, and Peter Schröder. 2013. Digital Geometry Processing with Discrete Exterior Calculus. In *ACM SIGGRAPH 2013 Courses (SIGGRAPH '13)*.

Keenan Crane, Mathieu Desbrun, and Peter Schröder. 2010. Trivial Connections on Discrete Surfaces. *Computer Graphics Forum* 29, 5 (2010).

Michel Crouzeix and Pierre-Arnaud Raviart. 1973. Conforming and nonconforming finite element methods for solving the stationary Stokes equations I. *ESAIM: Mathematical Modelling and Numerical Analysis - Modélisation Mathématique et Analyse Numérique* 7, R3 (1973), 33–75. http://eudml.org/doc/193250

Mark de Berg, Otfried Cheong, Marc van Kreveld, and Mark Overmars. 2008. *Computational Geometry: Algorithms and Applications* (3rd ed.). Springer-Verlag TELOS, Santa Clara, CA, USA.

Fernando de Goes, Mathieu Desbrun, Mark Meyer, and Tony DeRose. 2016b. Subdivision Exterior Calculus for Geometry Processing. *ACM Trans. Graph.* 35, 4, Article 133 (July 2016), 11 pages. https://doi.org/10.1145/2897824.2925880

Fernando de Goes, Mathieu Desbrun, and Yiying Tong. 2016a. Vector Field Processing on Triangle Meshes. In *ACM SIGGRAPH 2016 Courses (SIGGRAPH '16)*. ACM, New York, NY, USA, Article 27, 49 pages. https://doi.org/10.1145/2897826.2927303

M. Desbrun, A. N. Hirani, M. Leok, and J. E. Marsden. 2005. Discrete Exterior Calculus. (2005). preprint, arXiv:math.DG/0508341.

Olga Diamanti, Amir Vaxman, Daniele Panozzo, and Olga Sorkine-Hornung. 2014. Designing N-PolyVector Fields with Complex Polynomials. *Computer Graphics Forum* 33, 5 (2014).

Olga Diamanti, Amir Vaxman, Daniele Panozzo, and Olga Sorkine-Hornung. 2015. Integrable PolyVector Fields. *ACM Transactions on Graphics* 34, 4 (2015).

Michael Garland and Paul S. Heckbert. 1997. Surface Simplification Using Quadric Error Metrics. In *Proceedings of the 24th Annual Conference on Computer Graphics and Interactive Techniques (SIGGRAPH '97)*. ACM Press/Addison-Wesley Publishing Co., New York, NY, USA, 209–216. https://doi.org/10.1145/258734.258849

Eitan Grinspun, Petr Krysl, and Peter Schröder. 2002. CHARMS: A Simple Framework for Adaptive Simulation. *ACM Trans. Graph.* 21, 3 (July 2002), 281–290. https://doi.org/10.1145/566654.566578

Aaron Hertzmann and Denis Zorin. 2000. Illustrating smooth surfaces. In *Proc. SIGGRAPH 2000*.

Anil N Hirani. 2003. *Discrete exterior calculus*. Ph.D. Dissertation. California Institute of Technology.

Jinghao Huang and Peter Schröder. 2010. sqrt(3) -Based 1-Form Subdivision. In *Curves and Surfaces - 7th International Conference, Avignon, France, June 24-30, 2010, Revised Selected Papers*. 351–368. https://doi.org/10.1007/978-3-642-27413-8_22

T.J.R. Hughes, J.A. Cottrell, and Y. Bazilevs. 2005. Isogeometric analysis: CAD, finite elements, NURBS, exact geometry and mesh refinement. *Computer Methods in Applied Mechanics and Engineering* 194, 39 (2005), 4135–4195. https://doi.org/10.1016/j.cma.2004.10.008

Bert Jüttler, Angelos Mantzaflaris, Ricardo Perl, and Martin Rumpf. 2016. On numerical integration in isogeometric subdivision methods for PDEs on surfaces. *Computer Methods in Applied Mechanics and Engineering* 302 (2016), 131–146. https://doi.org/10.1016/j.cma.2016.01.005

Felix Kälberer, Matthias Nieser, and Konrad Polthier. 2007. QuadCover - Surface Parameterization using Branched Coverings. *Computer Graphics Forum* 26, 3 (2007).

Felix Knöppel, Keenan Crane, Ulrich Pinkall, and Peter Schröder. 2013. Globally optimal direction fields. *ACM Transactions on Graphics* 32, 4 (2013).

Bei-Bei Liu, Yiying Tong, Fernando de Goes, and Mathieu Desbrun. 2016. Discrete Connection and Covariant Derivative for Vector Field Analysis and Design. *ACM Transactions on Graphics* 35, 3 (2016).

Songrun Liu, Alec Jacobson, and Yotam Gingold. 2014. Skinning Cubic BÉZier Splines and Catmull-Clark Subdivision Surfaces. *ACM Trans. Graph.* 33, 6, Article 190 (Nov. 2014), 9 pages. https://doi.org/10.1145/2661229.2661270

Yang Liu, Helmut Pottmann, Johannes Wallner, Yong-Liang Yang, and Wenping Wang. 2006. Geometric Modeling with Conical Meshes and Developable Surfaces. *ACM Transactions on Graphics* 25, 3 (2006).

Charles Teorell Loop. 1987. *Smooth subdivision surfaces based on triangles*. Master's thesis, University of Utah, Department of Mathematics.

Michael Lounsbery, Tony D. DeRose, and Joe Warren. 1997. Multiresolution Analysis for Surfaces of Arbitrary Topological Type. *ACM Trans. Graph.* 16, 1 (Jan. 1997), 34–73. https://doi.org/10.1145/237748.237750

P Mullen, A McKenzie, D Pavlov, L Durant, Y Tong, E Kanso, JE Marsden, and M Desbrun. 2011. Discrete Lie advection of differential forms. *Foundations of Computational Mathematics* 11, 2 (2011).

Ashish Myles and Denis Zorin. 2012. Global Parametrization by Incremental Flattening. *ACM Transactions on Graphics* 31, 4 (2012).

Thien Nguyen, Keçstutis Karčiauskas, and Jörg Peters. 2014. A Comparative Study of Several Classical, Discrete Differential and Isogeometric Methods for Solving Poisson's Equation on the Disk. *Axioms* 3, 2 (2014), 280–299. https://doi.org/10.3390/axioms3020280

Konstantin Poelke and Konrad Polthier. 2016. Boundary-aware Hodge Decompositions for Piecewise Constant Vector Fields. *Comput. Aided Des.* 78, C (Sept. 2016), 126–136. https://doi.org/10.1016/j.cad.2016.05.004

Konrad Polthier and Eike Preuß. 2003. Identifying Vector Field Singularities Using a Discrete Hodge Decomposition. In *Visualization and Mathematics III*.

Hartmut Prautzsch, Wolfgang Boehm, and Marco Paluszny. 2002. *Bezier and B-Spline Techniques*. Springer-Verlag, Berlin, Heidelberg.

Nicolas Ray, Bruno Vallet, Wan Chiu Li, and Bruno Lévy. 2008. N-symmetry Direction Field Design. *ACM Transactions on Graphics* 27, 2 (2008).

Justin Solomon, Raif Rustamov, Leonidas Guibas, and Adrian Butscher. 2014. Earth Mover's Distances on Discrete Surfaces. *ACM Trans. Graph.* 33, 4, Article 67 (July 2014), 12 pages. https://doi.org/10.1145/2601097.2601175

Jos Stam. 2003. Flows on Surfaces of Arbitrary Topology. *ACM Trans. Graph.* 22, 3 (July 2003), 724–731. https://doi.org/10.1145/882262.882338

Gilbert Strang and George Fix. 2008. *An Analysis of the Finite Element Method*. Wellesley-Cambridge Press.

Bernhard Thomaszewski, Markus Wacker, and Wolfgang Strasser. 2006. A Consistent Bending Model for Cloth Simulation with Corotational Subdivision Finite Elements. In *Proceedings of the 2006 ACM SIGGRAPH/Eurographics Symposium on Computer Animation (SCA '06)*. Eurographics Association, Aire-la-Ville, Switzerland, Switzerland, 107–116. http://dl.acm.org/citation.cfm?id=1218064.1218079

Yiying Tong, Santiago Lombeyda, Anil N. Hirani, and Mathieu Desbrun. 2003. Discrete Multiscale Vector Field Decomposition. *ACM Transactions on Graphics* 22, 3 (2003), 445–452.

Amir Vaxman, Marcel Campen, Olga Diamanti, Daniele Panozzo, David Bommes, Klaus Hildebrandt, and Mirela Ben-Chen. 2016. Directional Field Synthesis, Design, and Processing. *Computer Graphics Forum* 35, 2 (2016), 545–572. https://doi.org/10.1111/cgf.12864

Ke Wang, Yiying Tong, Mathieu Desbrun, Peter Schröder, et al. 2006. Edge subdivision schemes and the construction of smooth vector fields. *ACM Transactions on Graphics* 25, 3 (2006).

Max Wardetzky. 2006. *Discrete Differential Operators on Polyhedral Surfaces–Convergence and Approximation.* Ph.D. Dissertation. Freie Universität Berlin.

Mirko Zadravec, Alexander Schiftner, and Johannes Wallner. 2010. Designing Quad-dominant Meshes with Planar Faces. *Computer Graphics Forum* 29, 5 (2010).

Eugene Zhang, Konstantin Mischaikow, and Greg Turk. 2006. Vector Field Design on Surfaces. *ACM Transactions on Graphics* 25, 4 (2006).

9. Appendices

A INNER PRODUCT ON Γ

In the following, we develop the inner product mass matrix M_Γ, to get the result of Equation 18.

Consider a face t with three edges e_A, e_B, e_C that are, without loss of generality, positively oriented towards the face. Further consider the associated halfedge forms $\gamma \in \Gamma$ restricted to the face on these edges: $\gamma_{1|A,B,C}$ and $\gamma_{2|A,B,C}$, representing respective vectors v_1 and v_2. They are packed on edges A and B, so to get the null-sum constraint $\gamma_{1|A} + \gamma_{1|B} + \gamma_{1|C} = 0$ (and resp. for γ_2) by definition. Following Equation 17, we have that the inner product M_Γ, restricted to the face, holds:

$$M_\Gamma = P^{-T} M_{\mathcal{F}} P^{-1},$$

so as to obtain the inner product in γ of the associated v on the face. We then get that:

$$M_\Gamma = P^{-T} M_{\mathcal{F}} P^{-1} = \frac{1}{4A_t^2} \begin{pmatrix} -e_B^\perp \\ e_A^\perp \end{pmatrix} \begin{pmatrix} A_t & & \\ & A_t & \\ & & A_t \end{pmatrix} \begin{pmatrix} -e_B^\perp \\ e_A^\perp \end{pmatrix}^T =$$

$$\frac{1}{4A_t} \begin{pmatrix} e_B^\perp \cdot e_B^\perp & -e_B^\perp \cdot e_A^\perp \\ -e_B^\perp \cdot e_A^\perp & e_A^\perp \cdot e_A^\perp \end{pmatrix}$$

Consider the angles $\alpha_{A|B|C}$ opposite to edges $e_{A|B|C}$. Then, we use the identities:

$$\frac{e_A^\perp \cdot e_A^\perp}{2A_t} = cot\left(\alpha_B\right) + cot\left(\alpha_C\right)$$
$$\frac{-e_A^\perp \cdot e_B^\perp}{2A_t} = cot\left(\alpha_C\right),$$

for any cyclic shift of $\left(A, B, C\right)$. Then we get:

$$M_\Gamma = \frac{1}{2} \begin{pmatrix} cot\left(\alpha_A\right) + cot\left(\alpha_C\right) & -cot\left(\alpha_C\right) \\ -cot\left(\alpha_C\right) & cot\left(\alpha_B\right) + cot\left(\alpha_C\right) \end{pmatrix} =$$

$$\frac{1}{2} Q^T \begin{pmatrix} cot\alpha_A & & \\ & cot\alpha_B & \\ & & cot\alpha_C \end{pmatrix} Q,$$

with the extension for all positive signs $Q = \begin{pmatrix} 1 & 0 \\ 0 & 1 \\ -1 & -1 \end{pmatrix}$.

B TEMPLATES FOR THE SUBDIVISION OPERATORS

We modified the integrated face-based subdivision $S_{\mathcal{F}^*}$ operator, derived from the DEC S_2 in SEC [de Goes et al. 2016b], to accommodate for our boundary conditions, and consequently had to modify S_1 around boundary vertices. In addition, we introduced a subdivision for unsigned integrated edge functions $S_{\mathcal{E}^*}$. We denote the vertex valence as d, including at the boundary, counting number of edges emanating from it (so regular boundary: $d = 3$).

B.1 Loop subdivision

$S_{\mathcal{V}}$ was chosen as Loop subdivision with

$$\alpha = \begin{cases} \frac{3}{8d}, & d \neq 3 \\ \frac{3}{16}, & d = 3, \end{cases} \tag{39}$$

as in [Biermann et al. 2000].The templates can be found in Figure 23. Similar to deGoes et al. [de Goes et al. 2016b], we chose to keep the odd stencil next to the boundary the same as the interior stencil.

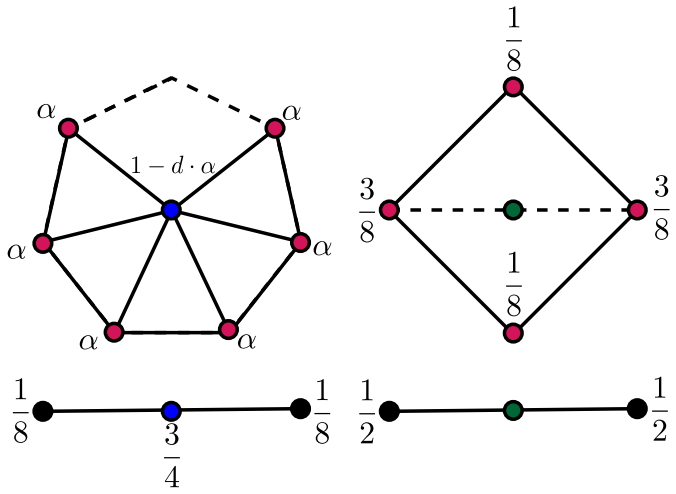

Fig. 23. Loop subdivision stencils used as $S_{\mathcal{V}}$ in our setting. d denotes the valence of the vertex.

B.2 Halfbox spline subdivision

For the halfbox spline subdivision operator $S_{\mathcal{F}}$, we use the same stencils as Wang et al. [Wang et al. 2006] for the interior faces, as given by Figure **??**. Due to the extra constraints on $S_{\mathcal{E}^*}$ at the boundary, we modified the boundary stencils for $S_{\mathcal{F}}$.

B.3 1-form subdivision operator

For completeness, we list the coefficients for the interior stencils of the S_1 subdivision operator, as used in deGoes et al. [de Goes et al. 2016b].

$$\eta_0 = \frac{3}{8} - \alpha - \frac{\beta}{4} \tag{40}$$

$$\eta_1 = \eta_{d-1} = \begin{cases} \frac{1}{8} - \alpha - \frac{\beta}{8} & d = 3, \\ \frac{1}{8} - \alpha & \text{otherwise} \end{cases} \tag{41}$$

$$\eta_2 = \eta_{d-2} = \begin{cases} \frac{\beta}{4} - \alpha & d = 4, \\ \frac{\beta}{8} - \alpha & \text{otherwise} \end{cases} \tag{42}$$

$$\theta_0 = -\theta_{d-1} = -\frac{\beta}{8} \tag{43}$$

$$\theta_1 = -\theta_{d-2} = \begin{cases} 0 & d = 3, \\ -\frac{\beta}{8} & \text{otherwise} \end{cases} \tag{44}$$

B.4 Stencil Constraints

The subdivisions were created with symmetric templates around the mesh elements where the quantities live, and were given the commutativity constraints:

$$\begin{aligned} d_0 S_{\mathcal{V}} &= S_1 d_1 \\ S_{\mathcal{F}^*} d_1 &= d_1 S_1 \\ S_{\mathcal{F}^*} A_{\mathcal{E}^* \to \mathcal{F}^*} &= A_{\mathcal{E}^* \to \mathcal{F}^*} S_{\mathcal{E}}^* \\ C_\Gamma S_\Gamma &= S_{\mathcal{E}^*} C_\Gamma \end{aligned}$$

B.5 Interior stencils

For constructing the interior stencils, we assume that the stencil coefficients are mirror symmetric with respect to the subdivided element. In addition, in correspondence with Wang et al., we fix the odd stencil for $S_{\mathcal{E}^*}$ with the same global shape as the S_1 odd stencil. Finally, we demand that the coefficients for even stencils of valence ≥ 7 are the same over the finite support of S_2.

After construction of the new $S_{\mathcal{E}^*}$ operator via the commutations, there are three degrees of freedom remaining. We resolve two of them by requiring all coefficients of the even valence 6 stencil to be positive. The remaining degree of freedom is present in the valence 4 even stencil, which we resolve by selecting the value that makes the dependent eigenvalue of the local subdivision matrix 116, which nicely fits the spectrum.

B.6 Boundary stencils

We assume all boundary stencils to be applied mirror symmetrically over the normal of the boundary.

Since we want to preserve the $C\gamma = 0$ condition on the boundary, we demand that the coefficients for the boundary stencil for even elements of $S_{\mathcal{E}^*}$ solely depend on the boundary.

In addition, we require that the odd stencil for the elements that touch the boundary with one of their vertices remains the same for $n \geq 3$.

Using the above assumptions on the stencils, we solve for $S_{\mathcal{E}^*}$, $S_{\mathcal{F}^*}$ and S_1 in conjunction. The resulting subdivision operators have a single degree of freedom left, which we resolve by requiring all $S_{\mathcal{F}^*}$ elements to be positive.

The Modified stencils for $S_{\mathcal{F}^*}$ is in Figure 24, for S_1 in Figure 25, and for $S_{\mathcal{E}^*}$ in Figure 26.

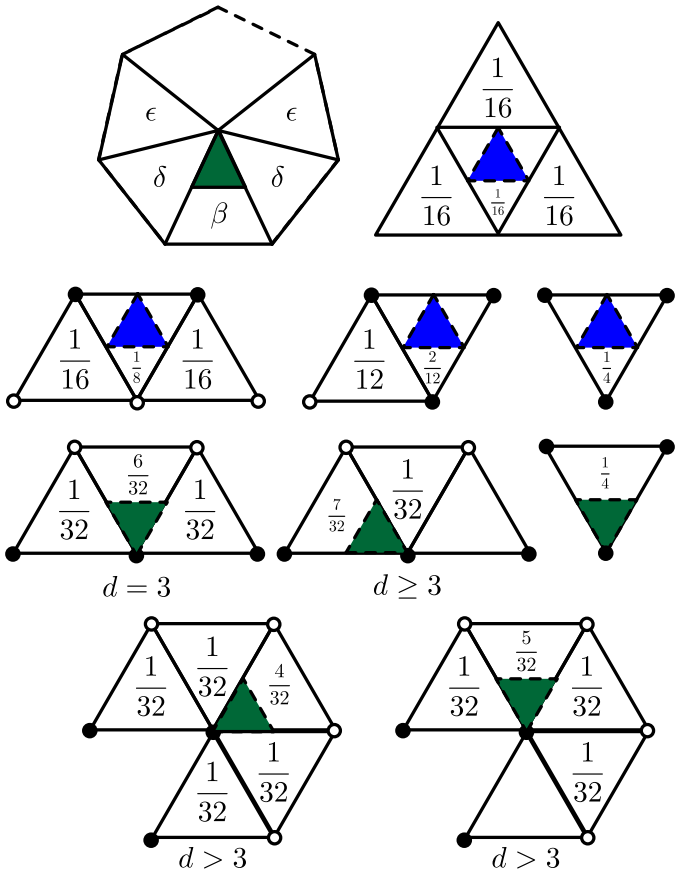

Fig. 24. Modified half-box splines subdivision operator $S_{\mathcal{F}^*}$.

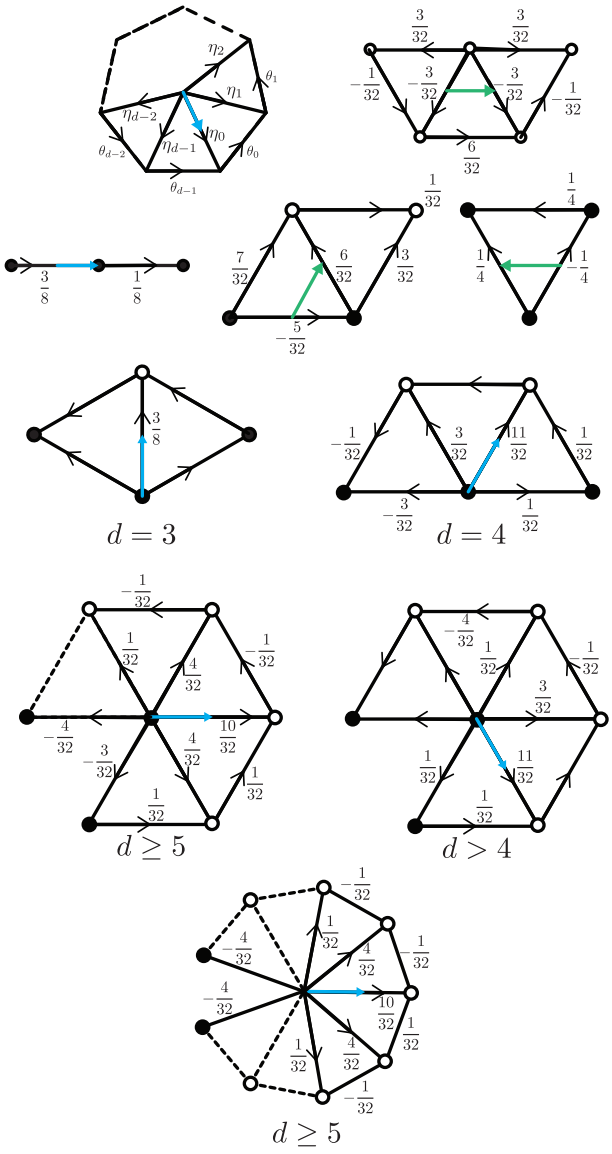

Fig. 25. 1-form subdivision operator S_1.

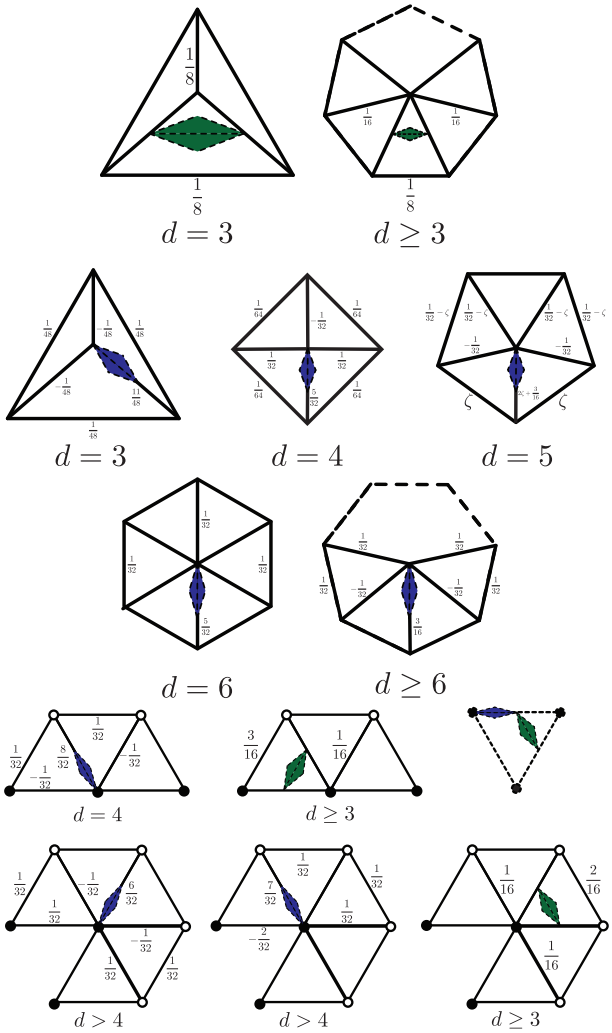

Fig. 26. Unsigned integrated edge subdivision $S_{\mathcal{E}^*}$.